Epitaxial Growth of High Quality InAs/GaAsSb Quantum Dots for Solar Cells

by

Yeongho Kim

A Dissertation Presented in Partial Fulfillment
of the Requirements for the Degree
Doctor of Philosophy

Approved September 2015 by the
Graduate Supervisory Committee:

Christiana Honsberg, Chair
Stephen Goodnick
Nikolai Faleev
David Smith

ARIZONA STATE UNIVERSITY

December 2015

ABSTRACT

The development of high efficiency III-V solar cells is needed to meet the demands of a promising renewable energy source. Intermediate band solar cells (IBSCs) using semiconductor quantum dots (QDs) have been proposed to exceed the Shockley-Queisser efficiency limit [1]. The introduction of an IB in the forbidden gap of host material generates two additional carrier transitions for sub-bandgap photon absorption, leading to increased photocurrent of IBSCs while simultaneously allowing an open-circuit voltage of the highest band gap. To realize a high efficiency IBSC, QD structures should have high crystal quality and optimized electronic properties. This dissertation focuses on the investigation and optimization of the structural and optical properties of InAs/GaAsSb QDs and the development of InAs/GaAsSb QD-based IBSCs.

In the present dissertation, the interband optical transition and carrier lifetime of InAs/GaAsSb QDs with different silicon delta-doping densities have been first studied by time-integrated and time-resolved photoluminescence (PL). It is found that an optimized silicon delta-doping density in the QDs enables to fill the QD electronic states with electrons for sub-bandgap photon absorption and to improve carrier lifetime of the QDs.

After that, the crystal quality and QD morphology of single- and multi-stack InAs/GaAsSb QDs with different Sb compositions have been investigated by transmission electron microscopy (TEM) and x-ray diffraction (XRD). The TEM studies reveal that QD morphology of single-stack QDs is affected by Sb composition due to strain reducing effect of Sb incorporation. The XRD studies confirm that the increase of Sb composition increases the lattice mismatch between GaAs matrix and GaAsSb spacers, resulting in increase of the strain relaxation in GaAsSb of the multi-

stack QDs. Furthermore, the increase of Sb composition causes a PL redshift and increases carrier lifetime of QDs.

Finally, the spacer layer thickness of multi-stack InAs/GaAsSb QDs is optimized for the growth of InAs/GaAsSb QD solar cells (QDSCs). The InAs/GaAsSb QDSCs with GaP strain compensating layer are grown and their device performances are characterized. The increase of GaP coverage is beneficial to improve the conversion efficiency of the QDSCs. However, the conversion efficiency is reduced when using a relatively large GaP coverage.

ACKNOWLEDGMENTS

I would like to thank my supervisory committee chair, Dr. Christiana Honsberg, for her motivation and encouragement during my graduate years. I was very fortunate to be a part of her research group. She provided me with an excellent and pleasant research environment. Under her guidance, I could focus on my scientific work without difficulties. Her valuable advice and insights on my research allowed me to broaden my research interests and solidify my research backgrounds. Additionally, I am much grateful to Dr. Nikolai Faleev who taught me MBE growth and XRD characterization. His strong research knowledge and experience helped me to grow high quality materials using MBE and to master XRD measurement and analysis. I would also like to thank Dr. David Smith and Dr. Dinghao Tang for TEM measurement and analysis. Their kind and useful feedback enriches the experimental results in my dissertation. I want to acknowledge Dr. Stephen Goodnick for his fundamental questions about my research topic, which helped to develop my research plan.

My special gratitude goes to Dr. Keun-Yong Ban who was one of our group members and is a great researcher. He truly helped me with scientific journal article writing. I would like to express my gratitude to Dr. Clarence Tracy for his constructive feedback on my research achievements. I deeply appreciate Dr. Darius Kuciauskas and Pat Dippo at National Renewable Energy Laboratory for PL measurement. I would also like to express my sincere gratitude to my lab colleague and friend, Chaomin Zhang. We worked with a III-V solar cell project for over two years and developed high efficiency solar cells. I want to acknowledge Yuan Zhao and Xiaomeng Shen of Dr. Yong-Hang Zhang's group for the help with PL and DLTS measurement.

Last but not least, I would like to acknowledge my parents and sisters in Korea for their unconditional love and support throughout my life. Thanks to their patience and sacrifice, I could accomplish my PhD studies.

TABLE OF CONTENTS

Page

CHAPTER Page

LIST OF TABLES

Table Page

LIST OF FIRGURES

Figure Page

Figure Page

Figure Page

Figure Page

Figure Page

Figure Page

Chapter 1

INTRODUCTION

1.1 Motivation

III–V compound semiconductor materials have been widely studied for high efficiency solar cell applications because their high absorption coefficient and wide range of bandgaps are beneficial for increased light absorption and hence photocurrent generation. In addition, their bandgaps can be adjustable to extend the absorption wavelengths by using ternary or quaternary alloy compounds. The detailed balance theory of Shockley and Queisser predicted the maximum conversion efficiency of ~30 % for single-junction solar cells with a bandgap of 1.1 eV under one-sun illumination (100 mW/cm^2) at AM 1.5G spectrum [1]. In order to overcome the thermodynamic efficiency limit of single-junction solar cells third generation solar cells, such as multijunction solar cells, intermediate band solar cells (IBSCs), and multiple exciton generation solar cells have been proposed and researched over the past two decades [2,3]. In particular, IBSCs are expected to have a maximum efficiency of 63.1 % under full concentration (46,050 suns) because the intermediate band (IB) allows three optical transitions of carriers to take place, as shown in Fig. 1.1 [2]. The first transition is between the valence band (VB) to the conduction band (CB), the second transition is between the VB to the IB, and the third transition is between the IB to the CB. The latter two transitions are induced by sub-bandgap photon absorption, which are additional paths to increase photocurrent of IBSCs.

Self-assembled InAs quantum dots (QDs) have been extensively investigated to realize high efficiency IBSCs because of their strong carrier confinement and high tunability of effective bandgap [4,5,6]. Their structural and electronic properties can be readily tuned by controlling growth conditions. Figure 1.2(a) shows a schematic

diagram of a QD-based IBSC where QDs are inserted in intrinsic region of a *p-i-n* solar cell structure. Under illumination conditions the confined carriers in QDs escape out of QDs which are located in a depletion region of an IBSC, as seen in Fig. 1.2(b) and they are then transported out of emitter and base regions, resulting in generating sub-bandgap photocurrent.

The device performance of the reported IBSCs with InAs/GaAs QD systems has been degraded than estimated by theoretical models for the following reasons despite a sub-bandgap photocurrent generation [6,7]. The most challenging issue is a significant reduction of the output voltage of IBSCs as a result of the introduction of InAs QDs with a narrow effective bandgap [7]. The voltage drop is enhanced by nonradiative recombination of carriers at strain-induced crystalline defects during QD growth. Furthermore, a large valence band offset (VBO) at the heterojunction between InAs QDs and GaAs barriers decreases the output voltage [8].

As an alternative to InAs/GaAs QDs, InAs/GaAsSb QDs have been recently suggested as a promising absorber material for IBSCs because of their many advantages [8, 9]. When Sb composition of GaAsSb barriers increases, the areal density of QDs increases whereas QD size decreases due to the surfactant effect of Sb [8]. Such small and dense QD morphologies help to increase QD absorption volume, leading to improved photocurrent generation. In addition, the Sb surfactant effect suppresses the formation of coalescent QDs and thereby the number of coherent QDs increases, accompanied with high QD size uniformity. Lastly, the energy band alignment at the heterointerface between InAs QDs and GaAsSb barriers can be tuned by increasing Sb composition. When the Sb composition exceeds ~14 % the band alignment changes from type-I to type-II line-up by shifting up valence band edges [9]. In type-II structure,

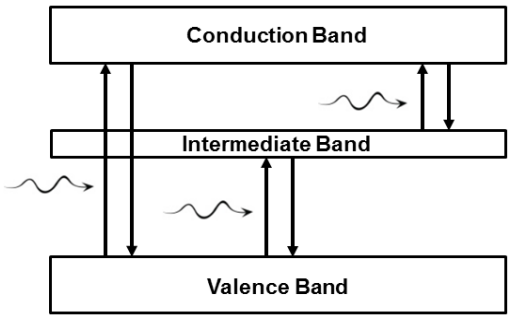

Fig. 1.1 Schematic of Three Carrier Transitions in Intermediate Band Solar Cells

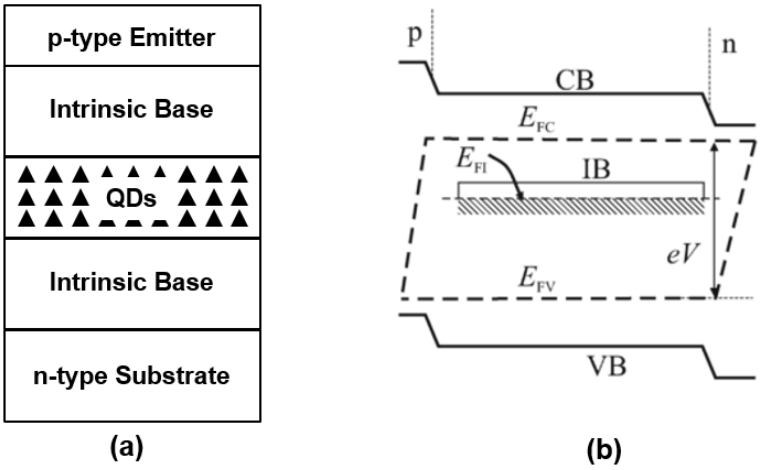

Fig. 1.2 (a) Schematic Structure of a *p-i-n* Intermediate Band Solar Cell with QDs Embedded in an Intrinsic Base Region and (b) its Energy Band Diagram in Equilibrium [4]

electrons are confined in InAs QDs while holes are localized in GaAsSb barriers. This carrier separation greatly decreases the probability of wavefunction overlap between carriers, leading to weak Columbic interaction and thus long carrier lifetime in QDs [10]. The improved carrier lifetime is required to avoid the loss of photocurrent of IBSCs.

These structural and optical properties of InAs/GaAsSb QDs are beneficial to improve the device performance of IBSCs. To use the QD systems as an active absorbing material of IBSCs, high-quality multi-stack QD layers need to be grown to create more photogenerated carriers. The InAs QDs surrounded by GaAsSb are compressively strained because the lattice constant of InAs is larger than that of GaAsSb. The multi-stacking of QDs increases the strain accumulation inside QDs, leading to generating crystalline defects such as misfit and threading dislocations. Figure 1.3 exhibits cross-sectional transmission electron microscopy (TEM) images of ten-stack InAs QD layers with varying InAs deposition coverages embedded in 25 nm-thick GaAs barriers [11]. The volcano-like defects are formed possibly due to sinusoidal gradient of surface chemical potential as strain accumulation is larger with increasing the number of QD layers. Moreover, the increase of InAs deposition coverage generates threading dislocations, as observed in Fig. 1.3(b), due to higher strain in the QDs. Therefore, strain engineering of QDs is greatly required to suppress the formation of the crystalline defects which act as nonradiative recombination centers.

Another critical issue related to the growth of high-quality InAs/GaAsSb QDs in GaAs matrix is increasing lattice mismatch between GaAs and GaAsSb with increasing Sb composition. As mentioned previously, the increase of Sb composition is favorable to increase carrier lifetime of QDs by the type conversion. However, a larger lattice mismatch at the interface of GaAs/GaAsSb with higher Sb composition can be

another source of crystalline defect generation as a result of strain relief in GaAsSb. In addition, the crystal quality of InAs QDs grown on dislocated GaAsSb surface can be degraded because dislocation trenches on the surface limits the migration of indium adatoms [12]. This leads to the poor QD size uniformity and reduction of the number of QDs.

Furthermore, the spacer layer thickness of GaAsSb in multi-stack InAs/GaAsSb QD structures has to be calibrated to generate an IB. The formation of an IB is crucial since it allows sub-bandgap photon absorption. As spacer thickness reduces the wavefunction overlap between electronic states of adjacent QD layers is enhanced. On the other hand, their crystal quality is poorer owing to strong strain accumulation in closely stacked QDs with thinner spacer thickness. In order to minimize the strain accumulation effect, strain compensation techniques can be applied by introducing GaP or GaAsN layers into QD stacks [13,14]. Therefore, it is important to understand the strain compensation effect on the structural and optical properties of multi-stack InAs/GaAsSb QDs.

Lastly, the photocarriers generated by sub-bandgap transitions should escape effectively out of the QDs under illumination condition for increasing photocurrent. The carriers confined in the QDs can jump out of QD potentials by thermal activation and can be trapped by InAs wetting layers, as shown in Fig. 1.4. When electron (hole) confinement is highly reduced, the open-circuit voltage of IBSCs is degraded owing to an insufficient quasi-Fermi separation between the IB and CB (VB) [15]. On the other hand, a high thermal stability of carriers can lead to strong carrier recombination without improving photocurrent, originating from an enhanced Coulombic interaction between carriers. Thus, a moderate thermal stability of carriers is required to boost

photocurrent and to avoid severe output voltage degradation by modifying structural and electronic structures of the QDs.

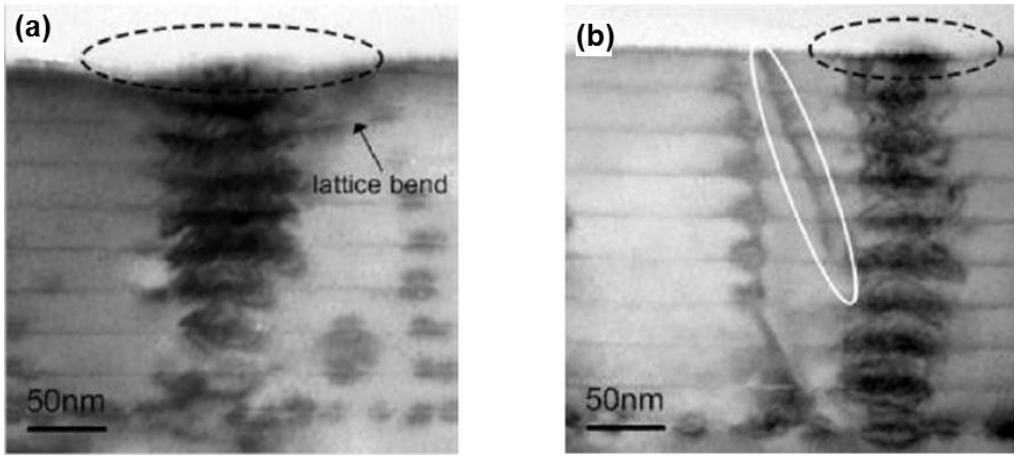

Fig. 1.3 Cross-sectional TEM Micrographs of Ten-stack InAs/GaAs QD Structures with Nominal InAs Deposition Coverages of (a) 2.73 ML and (b) 3.64ML (The Dotted and Solid Ellipse Indicate a Surface Degradation and Threading Dislocation, Respectively) [11]

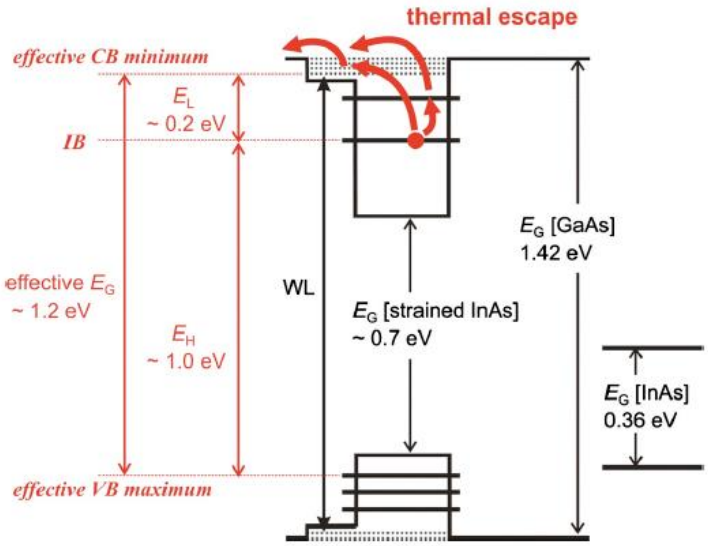

Fig. 1.4 Schematic Energy Band Diagram of InAs QD Capped with GaAs Layer [15]

1.2 Dissertation Outline

The electronic states of quantum dots (QDs) should be half-filled with electrons to absorb sub-bandgap photons and hence increase photocurrent in solar cell applications. To do this, silicon (Si) delta (δ)-doping has been introduced in type-II InAs/$GaAs_{0.83}Sb_{0.17}$ QDs and the optical properties of the QDs with different Si delta-doping densities have been investigated using photoluminescence (PL). The time-integrated PL measurement reveals that the QD ground state emission peaks are blueshifted with increasing Si doping density. It is estimated from the excitation power dependent PL measurement that the increase of Si doping density enhances radiative recombination rate of carriers, leading to a slower blueshift of the ground state peak energy with increasing the excitation power. Furthermore, the PL integrated intensity ratio of the ground state emission to the first excited state emission is increasing with increasing Si doping density. To study the thermal behavior of carriers, the temperature dependent PL measurement has been carried out in the temperature range of 10 to 300 K. The Si doping density is found to affect the redshift rate of the ground state peak energy with increasing temperature. The time-resolved PL exhibits that a moderate Si doping density helps to improve carrier lifetime of QDs. This will be addressed in Chapter 3.

The use of GaAsSb spacer layers has advantages in reducing strain in QDs and forming small and dense QDs, whereas it has disadvantages in increasing misfit strain at the GaAs/GaAsSb interfaces and changing QD morphology. Thus, it is important to study the effect of Sb composition on the crystal quality and luminescence properties of single- and multi-stack InAs/GaAsSb QDs. The increase of Sb composition in single-stack InAs/GaAsSb QDs slightly increases the aspect ratio of dots, which is defined as the ratio of dot height to diameter. This is due to the strain reducing effect of Sb. The

x-ray diffraction (XRD) measurement shows that the relaxation of initial elastic stress in GaAsSb layers of the multi-stack QDs increases with increasing Sb composition, which is ascribed to the higher lattice mismatch between GaAs and GaAsSb layers. In addition, the PL emission peak energy of the QDs is redshifted with increasing Sb composition because QDs are less strained, resulting from the reduced lattice mismatch between InAs and GaAsSb layers. The time-resolved PL measurement reveals that the carrier lifetime in the QDs is increasing with increasing Sb composition since Sb incorporation decreases the valence band offset at the heterointerface between InAs and GaAsSb, leading to a weak hole confinement. This will be addressed in Chapter 4.

When growing multi-stack InAs/GaAsSb QDs as a sub-bandgap photon absorber for intermediate band solar cells, spacer layer thickness of GaAsSb has to be precisely calibrated since it affects strain field distribution in QD stacks and hence modifies QD properties. The structural and optical properties of ten-stack InAs/GaAsSb QDs with different GaAsSb spacer layer thicknesses has been characterized by XRD, transmission electron microscopy (TEM), and PL. The degree of strain relaxation in spacer layers increases with increasing spacer layer thickness. The crystalline defect density of GaAsSb layers is highly affected by spacer layer thickness. The PL emission peak energy of QDs shows a nonmonotonous shift with increasing spacer layer thickness, which is a result of the competing effects of PL redshift and blueshift. This will be addressed in Chapter 5.

The multi-stack InAs QDs are highly in-plane compressive-strained since strain accumulation inside QDs increases with increasing the number of QD layers. The compressive strain of QDs can be effectively compensated by introducing a tensile strain of strain compensating layers such as GaP. The material properties and device performances of InAs/GaAsSb quantum dot solar cells (QDSCs) with different GaP

coverages have been investigated. The XRD study demonstrates that the compressive strain of QDs decreases with increasing GaP coverage. The reduced compressive strain causes PL peak energy redshift of QDs, whereas PL peak blueshift is induced by a high potential barrier effect of GaP. When GaP coverage increases from 1 to 4 ML, the sub-bandgap photocurrent by QD absorption decreases. Furthermore, the conversion efficiency of the QDSCs increases with increasing GaP coverage up to 2 ML. However, a further increase of GaP coverage to 4 ML degrades the conversion efficiency due to an increased elastic stress of GaP. This will be addressed in Chapter 6.

The original contribution of this dissertation is optimizing the structural and electronic properties of InAs QDs embedded GaAsSb strain reducing layers for QDSCs. To do this, Si δ-doping, Sb composition and spacer thickness of GaAsSb have been systematically calibrated. From the growth and characterization of InAs QDs with these growth parameters, multi-stack InAs/GaAsSb QD structures have been optimized. To further reduce strain accumulation in the optimized QDs, GaP strain compensation layers have been introduced in the QD stacks and InAs/GaAsSb QDSCs with different GaP coverages have been first fabricated. The research results in this dissertation demonstrate the feasibility of improving the device performance of InAs/GaAsSb QDSCs.

Chapter 2

BACKGROUND

2.1 Fundamentals of Quantum Dots

2.1.1 Self-assembled Quantum Dots

Semiconductor materials grow when adsorbed atoms condense on a surface of wafer through three growth modes of Frank-van der Merwe (F–M), Volmer-Weber (V–W), and Stranski-Krastanov (S–K) [16]. These growth modes are related to surface and interface free energy, which depend on surface and interface tension of materials. As illustrated in Fig. 2.1, two dimensional layer-by-layer growth becomes possible via the F–M mode under the condition of $\gamma_s > \gamma_f + \gamma_{s\text{-}f}$, where γ_s is the surface free energy of substrate, γ_f is the surface free energy of film, and $\gamma_{s\text{-}f}$ is the interface free energy between substrate and film. In V–W mode, three dimensional islands are grown without two dimensional layer growth under the condition of $\gamma_s < \gamma_f + \gamma_{s\text{-}f}$. Two dimensional layer-by-layer growth changes to three dimensional island growth in S–K mode, which is a mixed mode of the F–M and V–W. In S–K mode, the strain energy of $\gamma_f + \gamma_{s\text{-}f}$ is low with a small amount of deposition coverage of film. The increase of film deposition coverage increases $\gamma_f + \gamma_{s\text{-}f}$, resulting in the condition of $\gamma_s < \gamma_f + \gamma_{s\text{-}f}$.

Self-assembled quantum dots (QDs) are grown with highly lattice-mismatched materials under a crystallographic equilibrium state using the S–K growth mode. Figure 2.2 displays the formation sequence of InAs QDs on GaAs layers. The lattice mismatch, $f = (a_{InAs} - a_{GaAs})/a_{GaAs}$, between InAs and GaAs is ~7.2 % at room temperature, where a_{InAs} (= 6.058 Å) and a_{GaAs} (= 5.653 Å) are the lattice constants of InAs and GaAs, respectively. When InAs is deposited on GaAs at the initial growth stage, 1 monolayer (ML) high two-dimensional (2D) wetting layer (WL) is formed on GaAs surface. Due to the high lattice mismatch strain, InAs is in-plane compressive-strained whereas GaAs

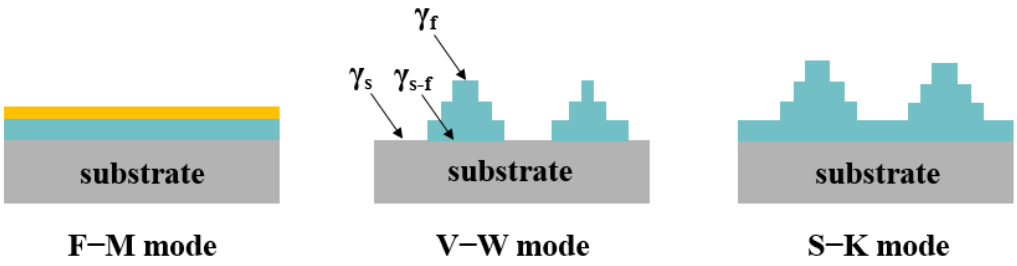

Fig. 2.1 Three Growth Modes of Frank–Van der Merwe (F–M), Volmer–Weber (V–W), and Stranski–Krastanov (S–K)

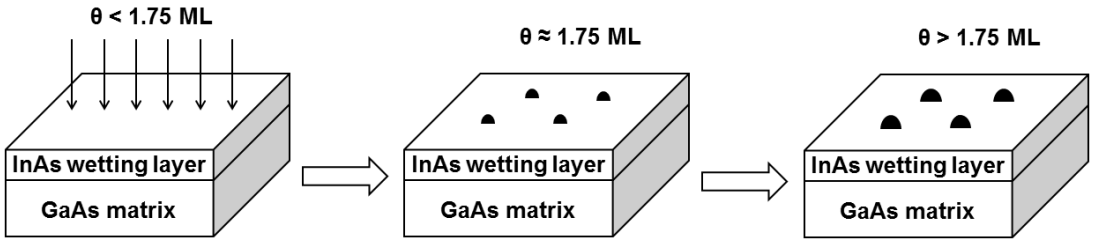

Fig. 2.2 Morphological Evolution of InAs QDs with InAs Deposition Coverage, θ, Grown by S–K Growth Mode

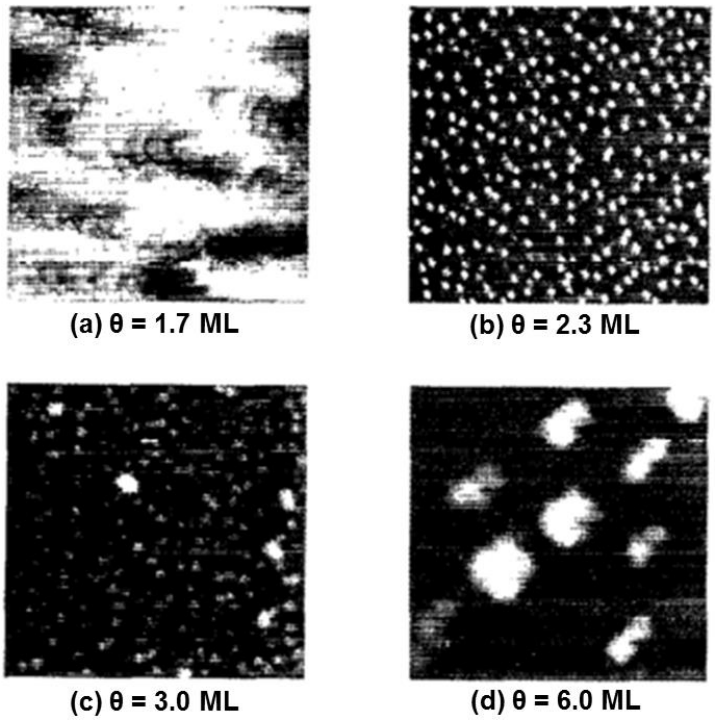

Fig. 2.3 Atomic Force Microscopy Images (1×1 μm^2) of InAs QDs on GaAs with Different InAs Deposition Coverages, θ, of (a) 1.7 ML, (b) 2.3 ML, (c) 3.0 ML, and (d) 6.0 ML [17]

is in-plane tensile-strained with increasing the deposition coverage of InAs. The InAs QD nucleation begins when the InAs deposition coverage approaches ~1.75 ML with increasing misfit strain energy [17]. The elastic strain in InAs is then relaxed to reduce the strain energy, accompanied by the formation of three-dimensional (3D) InAs QDs. During the relaxation process, crystalline defects are usually generated at InAs QD/GaAs barrier interfaces. The further increase of InAs deposition coverage increases QD sizes of diameter and height due to material gain, as shown in Fig. 2.3**.**

It should be noted that QD morphology can change significantly during QD capping process. Figure 2.4 shows cross-sectional scanning tunneling microscopy images of InAs QDs capped with different capping layers of GaAsSb and GaAs [18]. In the topography images, the shape of GaAsSb-capped QDs is pyramidal while that of GaAs-capped QDs is truncated. The QD capping with GaAs enhances strain accumulation since the lattice constant of GaAs is smaller than that of GaAsSb, as shown in Fig. 2.5. The increased strain decomposes In-As bonding of GaAs-capped QDs and causes indium surface segregation out of QDs, leading to the formation of truncated shaped dots. The change in QD morphology during the growth directly affects electronic and optical properties of QDs since it modifies the strain field distribution in QDs, which will be addressed below.

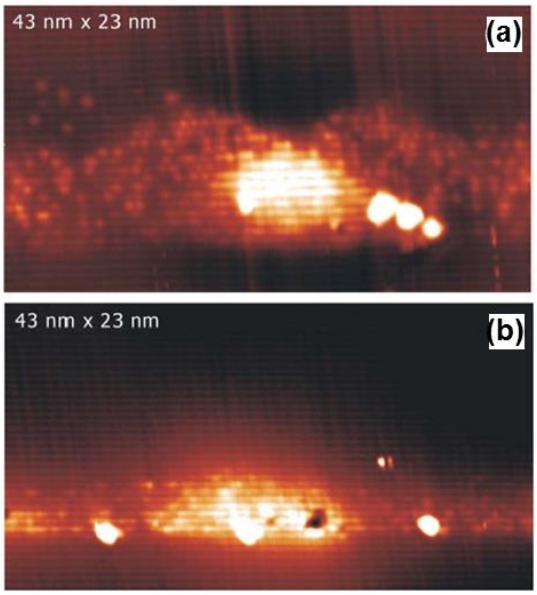

Fig. 2.4 Cross-sectional Scanning Tunneling Microscopy Images of InAs QDs Capped with (a) GaAsSb and (b) GaAs [18]

.

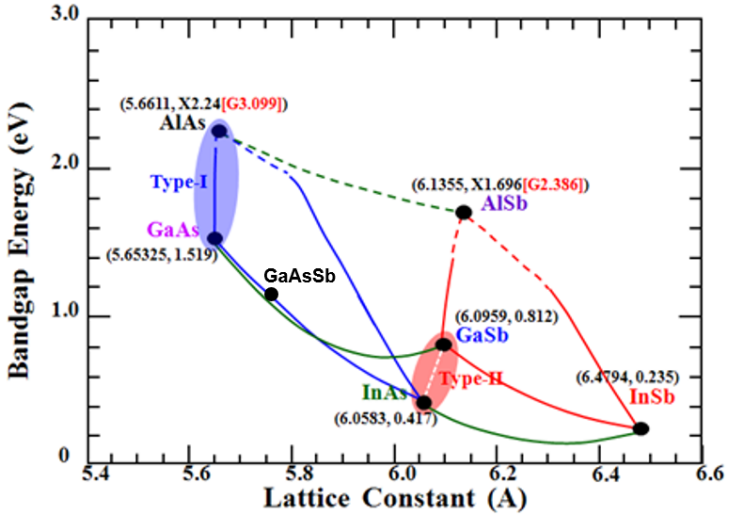

Fig. 2.5 Relationship between Bandgap Energy of III-V Materials and Their Lattice Constant at 0 K

2.1.2 Structural and Electronic Properties

QDs have shown unique electronic and optical properties which originate from their small feature size. Typical sizes of InAs QDs are 20–50 nm in diameter and 5–10 nm in height. The QD dimensions are less than the de Broglie wavelength, λ_B, of electrons and holes in InAs, which is expressed by

$$\lambda_B = \frac{2\pi\hbar}{\sqrt{3k_B Tm^*}} \tag{2.1}$$

where $\hbar$ is the reduced Planck's constant, k_B is the Boltzmann constant, T is temperature, and m^* is the effective mass of carriers. The carriers in InAs QDs are strongly confined in all three-dimensional directions, as seen in Fig. 2.6(a). Therefore, QDs are referred to as a zero-dimensional system because carriers confined in QDs have zero degree of freedom. This zero-dimensionality causes delta-function-like density of states (DOS), *g(E)*, of QDs, which is given by the following relations [19] and it is plotted in Fig. 2.6(b).

$$g(E) = \sum_{l,m,n}\left(\frac{1}{L_x L_y L_z}\right)\delta[E-(E_l+E_m+E_n)] \tag{2.2}$$

$$E_{l,m,n} = \frac{\pi^2\hbar^2}{2m^*}\left(\frac{l^2}{L_x^2}+\frac{m^2}{L_y^2}+\frac{n^2}{L_z^2}\right) \qquad l,m,n = 1,2,3,... \tag{2.3}$$

However, the DOS of QDs is broadened by QD size fluctuation, which is inevitable in S–K QD growth mode.

In addition, electronic structure of QDs is affected by strain field modification during QD capping process. Figure 2.7(a) shows the band structure of unstrained InAs, calculated by nonlocal pseudopotential method [20]. At the Γ point the fundamental bandgap, E_g, of unstrained InAs is 0.37 eV and spin-orbit split-off energy gap, E_{so}, is 0.43 eV. Further, the heavy and light hole bands are not split. However, they are split and E_g increases when QDs

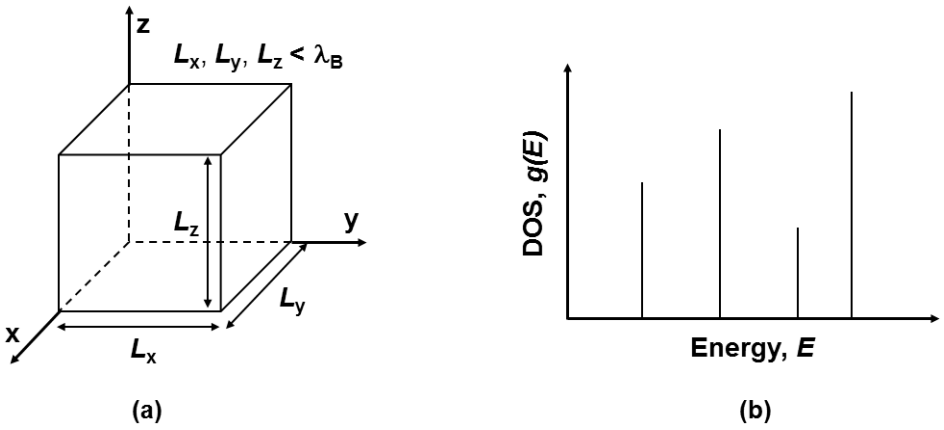

Fig. 2.6 (a) Schematic of an Individual QD Confined in Three-dimensional Directions (b) its Delta-function-like Density of States with Different Numbers of Degeneracies

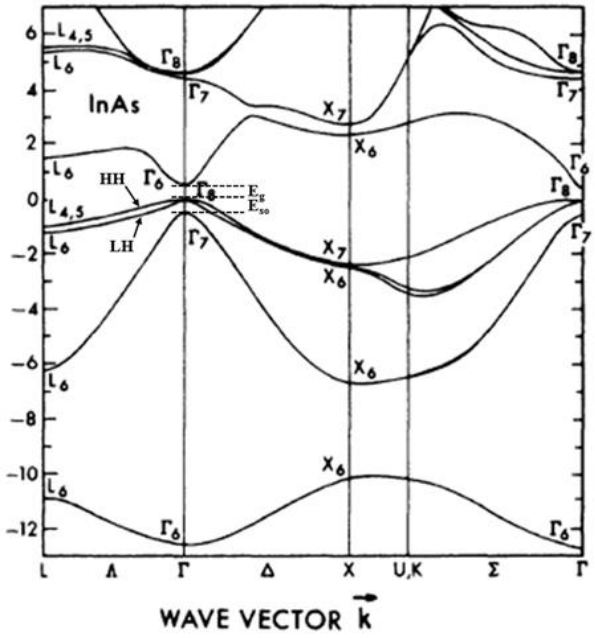

Fig. 2.7 (a) Theoretical Band Structure of InAs (HH and LH Indicate Heavy and Light Hole Bands, Respectively.) [20] (b) Strain Effect on InAs Band Structure

are strained after capping with barrier materials, as seen in Fig. 2.7(b). The electronic band structure of strained QDs can be calculated with the eight-band $\boldsymbol{k}\cdot\boldsymbol{p}$ theory including the strain effect. According to the theory, the strain in pyramidal shaped QDs induces an energy shift of conduction band edge energy by ΔE_c [21]

$$\Delta E_C(\varepsilon) = E_{C,str.} - E_{C,unstr.} = a_C(\varepsilon_{xx} + \varepsilon_{yy} + \varepsilon_{zz}) \tag{2.4}$$

where $E_{c,str.}$ and $E_{c,unstr.}$ are conduction band edge energies of strained and unstrained InAs, respectively, a_c is the deformation potential of conduction band at the Γ point, and ε is the strain component. The heavy (E_{hh}) and light (E_{lh}) hole band edge energies are nondegenerated as follows.

$$E_{hh} = a_v\varepsilon_h - b\varepsilon_b + (E_v + \frac{\Delta_{SO}}{3}) \tag{2.5}$$

$$E_{lh} = a_v\varepsilon_h + \frac{1}{4}b\varepsilon_b + E_v - \frac{\Delta_{SO}}{6} + \frac{1}{2}\sqrt{\Delta_{SO}^2 + \left(\Delta_{SO} + \frac{9}{4}\right)b\varepsilon_b} \tag{2.6}$$

where a_v and b are the hydrostatic and shear deformation potentials of valence band, respectively, ε_h is the hydrostatic strain ($=\varepsilon_{xx}+\varepsilon_{yy}+\varepsilon_{zz}$), ε_b is the biaxial strain ($=\varepsilon_{zz}-(\varepsilon_{xx}+\varepsilon_{yy})/2$), E_v is the average valence band energy, and Δ_{SO} is the spin-orbit split-off energy. According to Eqs. (2.4)−(2.6), when InAs is in-plane compressive-strained, the conduction band edge is shifted upward and heavy and light hole band edges are split.

It is also noted that interband and intersubband optical transitions in QDs can be tuned by changing the size or shape of QDs. Furthermore, the optical transitions of InAs QDs are affected by In/Ga intermixing at the heterointerface between InAs QDs and GaAs barriers. Figure 2.8 shows the photoluminescence spectra at 10 K of InAs/GaAs QDs under different rapid thermal annealing (RTA) temperatures, ranging from 700 to 950℃ [22]. As RTA temperature increases, the interband transition

energies of E_0, E_1, and E_2 increase while the intersubband transition energies of E_1-E_0 and E_2-E_1 decrease. This is due to the intermixing of In/Ga atoms at the InAs QD/GaAs barrier interfaces. The RTA induces the diffusion of Ga atoms into the QDs and they are incorporated in InAs QDs. The increase of Ga concentration in the QDs increases the QD effective bandgap, and in turn increases the interband transition energy [22]. In addition, the aspect ratio of QDs can be reduced with increasing In/Ga intermixing, resulting in decreasing the intersubband transition energy since it strongly affects the strain tensors [23,24].

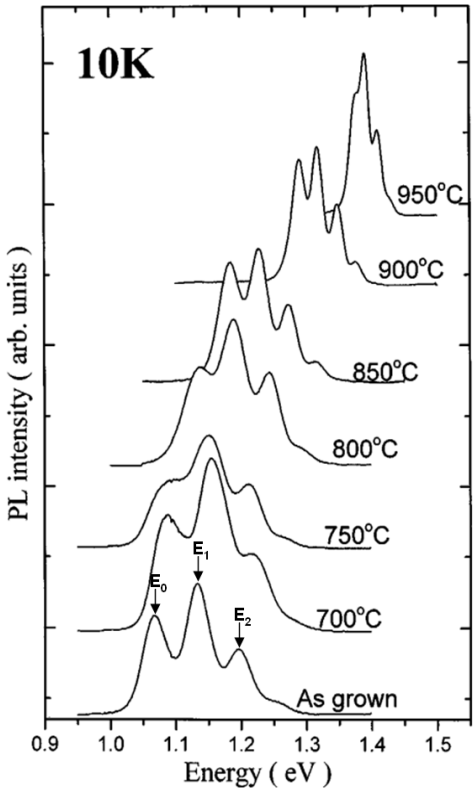

Fig. 2.8 Photoluminescence Spectra of InAs QDs at 10 K under Different RTA Temperatures. E_0, E_1, and E_2 Indicate the Interband Optical Transitions at the Ground States, First Excited States, and Second Excited States, Respectively [22]

2.2 Molecular Beam Epitaxy for Quantum Dots Growth

Molecular beam epitaxy (MBE) is a state-of-the-art technique to grow high quality epitaxial layers under ultra-high vacuum condition. MBE allows growth of various nanostructures such as quantum wells, quantum wires, and quantum dots. When a solid source in an effusion cell is heated up, molecular beams are produced and they are transported into the substrate rotating in a growth chamber. Then, they diffuse on the heated substrate surface and combine with other species of atoms, leading to binary, tertiary, or quaternary alloys.

Figure 2.9(a) shows a schematic of a typical MBE system. The MBE system consists of three main systems: vacuum system, growth chamber system, and reflection high energy electron diffraction system.

1) *Vacuum system*: An ultra high vacuum (UHV) system is required to reduce partial pressure of impurities in an MBE system. Furthermore, it helps to increase a mean free path of molecular beams, which enables them to impinge unreacted on the substrate surface. To maintain UHV conditions, MBE chambers are connected to several pumps such as ion pumps, titanium sublimation pumps, and cryogenic pumps. In addition, the growth chamber is surrounded by liquid nitrogen cryopanels which suppress re-evaporation of impurities attached on inner walls of the growth chamber.

2) *Growth chamber system*: The growth chamber system consists of effusion cells, shutters, substrate manipulator, ion gauges, and quadrupole mass spectrometer, as shown in Fig. 2.9(b). Effusion cells contain source crucibles which are made from pyrolytic boron nitride with high thermal and chemical stabilities. The molecular beam fluxes from effusion cells have to be highly stable by minimizing the variation of effusion cell temperatures. The tantalum or molybdenum pneumatic shutters in front of effusion cells are installed in order to trigger molecular beam fluxes. Substrate

manipulator is used to heat and rotate the substrate. During MBE growth, the substrate is heated to supply thermal energy required for the nucleation and condensation of adatoms and rotated for deposition uniformity. The molecular beam fluxes and growth chamber base pressure are monitored by ion gauges. A quadrupole mass spectrometer measures partial pressures of background residual species in the growth chamber.

3) *Reflection high energy electron diffraction system*: Reflection high energy electron diffraction (RHEED) system is a powerful in-situ tool to monitor surface states such as surface periodicity and surface reconstruction of samples. Figure 2.10(a) shows the intensity of specular RHEED spot according to time evolution and shows that the RHEED intensity oscillates periodically [25]. At a deposition coverage of $\theta = 0$ ML, the reflection from a smooth surface is maximum, leading to the highest specular spot intensity. As the deposition coverage increases to 0.25 ML, the spot intensity is reduced because of a surface roughness, which limits the surface reflection. Further increase of deposition coverage to 0.5 ML leads to the lowest spot intensity. When the deposition coverage approaches 1 ML, the spot intensity is recovered to the maximum. From the RHEED oscillation, the growth rate of epitaxial layers can be evaluated by dividing 1 ML by the time difference between two adjacent peaks with maximum spot intensity. The grazing incidence of electron beams from a RHEED gun increases elastic scattering cross-section and decreases penetration depth as seen in Fig. 2.10(b). The RHEED patterns are observed when reciprocal lattice rods of surface structures intercept the Ewald sphere. From a RHEED geometry, a surface periodicity, *a*, can be determined using the following relation.

$$a = \sqrt{h^2 + k^2}\,\frac{\lambda L}{S} \tag{2.7}$$

where h and k are the Miller indices, λ is the electron wavelength, L is the horizontal distance between sample and RHEED screen, and S is the spatial separation between

adjacent streak RHEED patterns. According to the relation, the surface periodicity is inversely proportional to the streak spacing. In addition, surface reconstruction of samples can be monitored by RHEED. Adatoms on a surface of sample rearrange themselves in ways that help to reduce the surface energy of crystals. Figure 2.11(a) illustrates the four types of (2×4) surface reconstructions of GaAs (001) surface [26] and their corresponding RHEED patterns are shown in Fig. 2.11(b) [27].

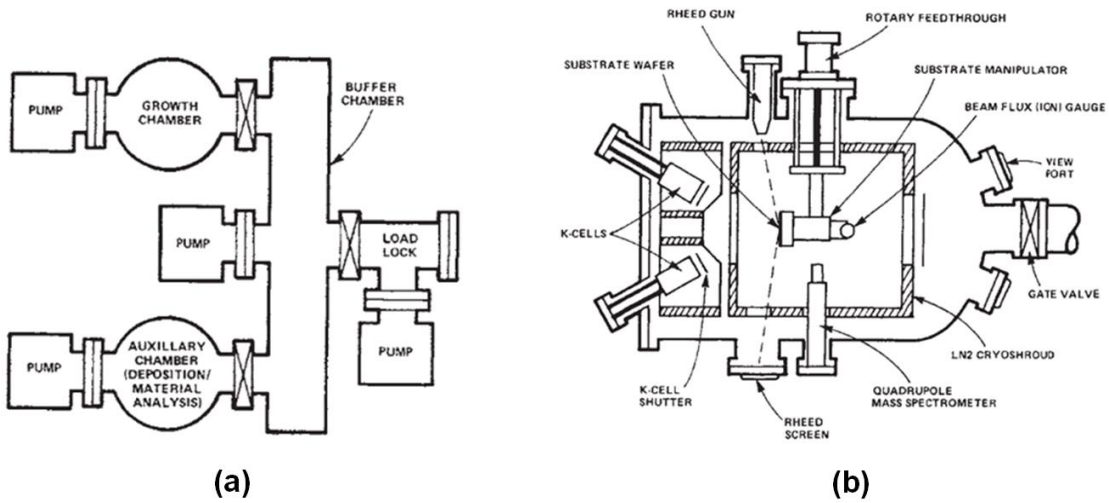

Fig. 2.9 (a) Schematic of a Typical MBE System and (b) MBE Growth Chamber [25]

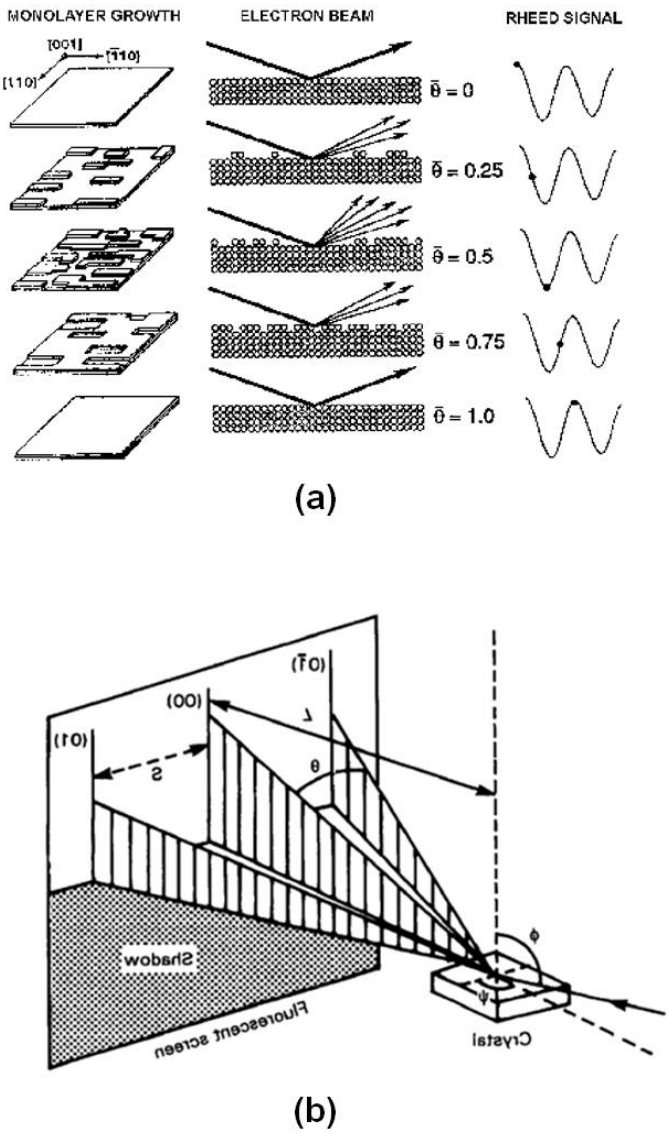

Fig. 2.10 (a) Schematic of a RHEED Oscillation During Layer-by-layer Growth and (b) RHEED Geometry [26]

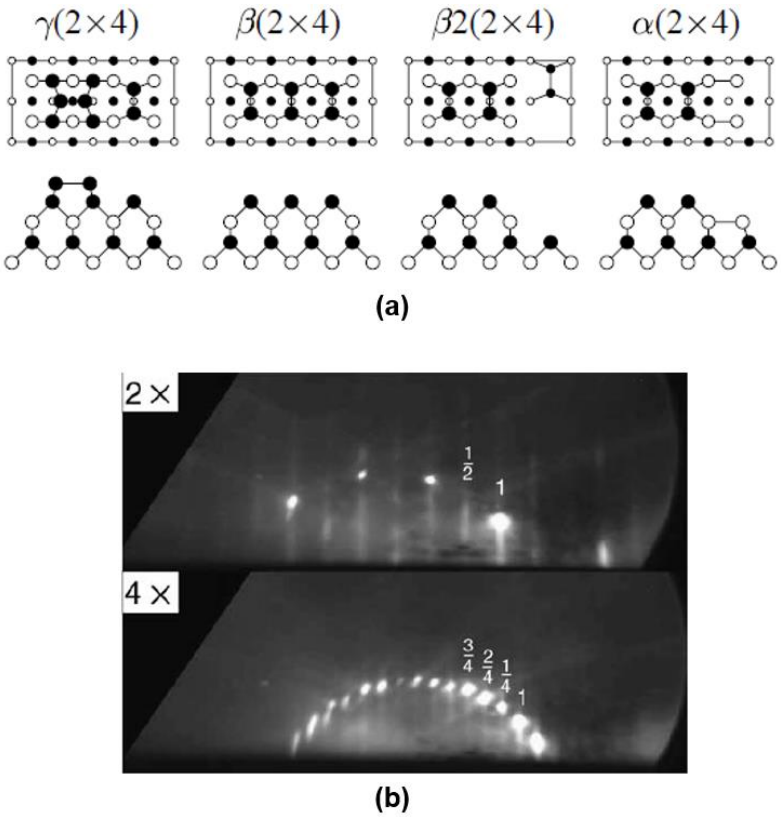

Fig. 2.11 (a) GaAs (001)-(2×4) Surface Reconstruction (Filled and Empty Circles Represent As and Ga, Respectively) [27] (b) (2×4) RHEED Patterns for GaAs (001) Surface Reconstruction [28]

2.3 Solar Cell Fundamentals

2.3.1 Device Operation of Solar Cells

Solar cells produce electricity by absorbing photons with energies, which are greater than those of host materials. The fundamental operation principle of solar cells is illustrated in Fig. 2.12(a). The photons are incident on a host semiconductor material and they generate electron-hole pairs. Then, the excited carriers diffuse through the host semiconductor and finally they are collected at the exterior contacts, leading to creating electrical current.

To develop high efficiency solar cells, it is important to understand energy loss processes in solar cells. Solar cells are unable to absorb photons with energies, which are less than the bandgap of host materials. On the other hand, the photons with much higher energies can be absorbed by solar cells and they excite electron-hole pairs. Then, the energetic carriers thermalize quickly and they are positioned at band edge states, resulting in lattice vibration (i.e. heating solar cells). In addition, photocarriers can radiatively recombine as seen in Fig. 2.12(b). Such band-to-band recombination does not contribute to photocurrent generation in solar cells. Furthermore, photocarriers can be trapped at crystalline defects, which act as nonradiative recombination centers. This trap-assisted recombination, which is known as Shockley-Read-Hall recombination, causes the degradation of photocurrent and output voltage of QD-based IBSCs [29]. Besides, absorption loss caused by light reflection from a front surface of solar cells, series resistance of host material, and contact resistance between host material and electrodes are critical factors, limiting the solar cell performance.

Solar cell performance is characterized by analyzing the main parameters of short-circuit current density (J_{sc}), open-circuit voltage (V_{oc}), fill factor (FF), conversion

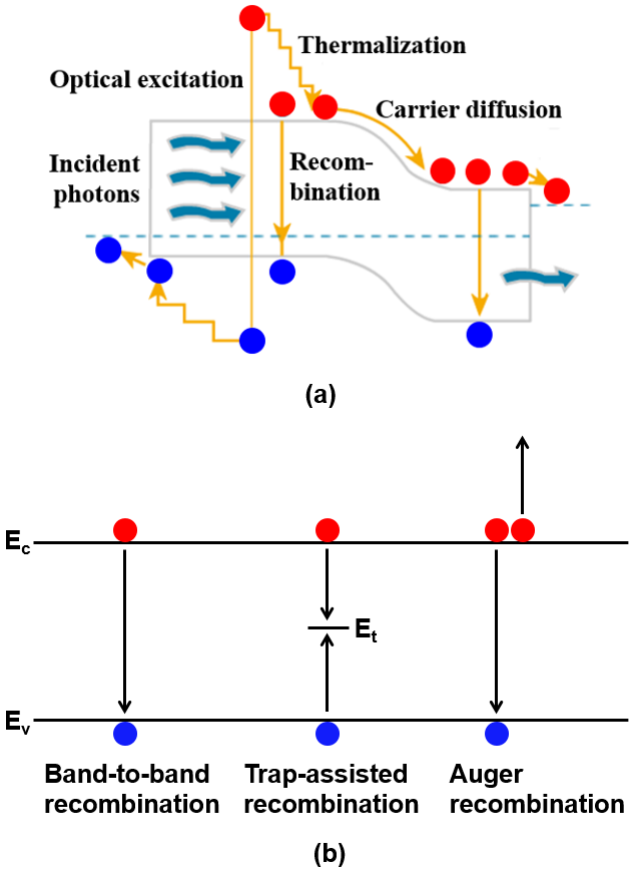

Fig. 2.12 (a) Fundamental Operation Principle of Solar Cells and (b) Recombination Mechanisms between Electrons and Holes in Semiconductors (E_c, E_v, and E_t Denote the Conduction Bandedge, Valence Bandedge, and Trap Level, Respectively)

efficiency (η), and external quantum efficiency (EQE). The voltage dependent current density, J(V), of solar cells can be expressed by

$$J(V) = J_0\left[\exp\left(\frac{qV}{k_B T}\right) - 1\right] - J_{ph} \tag{2.8}$$

where J_0 is the reverse bias saturation current density, q is the electron charge, k_B is the Boltzmann constant, T is the operating temperature, and J_{ph} is the photocurrent of solar cells. The J_{sc} is the current density flowing through solar cells when they are short-circuited (V = 0) under an illumination condition. It is noted that most of solar cells have series and shunt resistances, which highly affect the J(V). Figure 2.13(a) illustrates an equivalent circuit of a solar cell with series and shunt resistances and the J(V) can be expressed by

$$J(V) = J_0\left[\exp\left(\frac{q(V - AJR_s)}{k_B T}\right) - 1\right] + \frac{V - AJR_s}{R_{sh}} - J_{ph} \tag{2.9}$$

where R_s is the series resistance, R_{sh} is the shunt resistance, and A is the solar cell area. The V_{oc} is the maximum output voltage under the condition of J(V) = 0 and can be evaluated by

$$V_{oc} = \frac{k_B T}{q}\ln\left(\frac{J_{ph}}{J_0} + 1\right) \tag{2.10}$$

As clearly seen in the equation, V_{oc} is correlated with J_{ph} and J_0. The increase of crystalline defects decreases J_{ph} and increases J_0. Accordingly, V_{oc} is highly reduced when crystal quality of solar cells is deteriorated. As shown in Fig. 2.13(b), the FF is the ratio between the maximum power from a solar cell and the product of J_{sc} and V_{oc}.

$$FF = \frac{J_{mp} \times V_{mp}}{J_{sc} \times V_{oc}} \tag{2.11}$$

where J_{mp} and V_{mp} is the current density and output voltage at the maximum power point. The empirical FF can be expressed as follows [30].

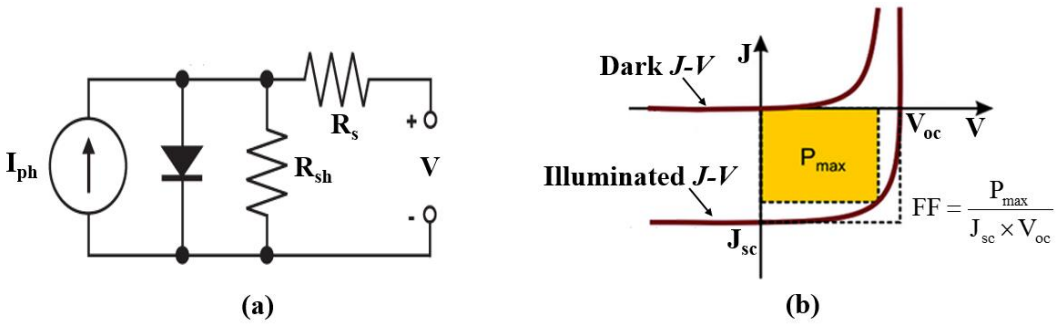

Fig. 2.13 (a) Equivalent Circuit of a Solar Cell and (b) Fill Factor of a Solar Cell under Illumination Condition

$$FF = \frac{v_{oc} - \ln(v_{oc} + 0.72)}{v_{oc} + 1} \tag{2.12}$$

$$v_{oc} = \frac{q}{nk_B T} V_{oc} \tag{2.13}$$

where v_{oc} is the normalized V_{oc} and n is the diode ideality factor. Thus, the increase of solar cell ideality factor decreases FF as well as V_{oc}. The η is defined as the ratio between the maximum converted power (P_{max}) and incident power (P_{in} = 100 mW/cm^2 at AM 1.5G spectrum.

$$\eta = \frac{P_{max}}{P_{in}} = \frac{J_{sc} \times V_{oc} \times FF}{P_{in}} \tag{2.14}$$

The EQE is the ratio of the number of photogenerated electron-hole pairs collected at the electrodes to the number of incident photons. The wavelength dependent EQE can be described as follows.

$$EQE(\lambda) = \frac{I_{ph}(\lambda)}{q\Phi_{ph}(\lambda)} \tag{2.15}$$

where I_{ph} is the voltage dependent photocurrent and Φ_{ph} is the incident photon flux. From EQE measurement, J_{sc} of a solar cell with a cell area of A can be determined by

$$J_{sc} = qA\int_{\lambda_1}^{\lambda_2} EQE(\lambda)\Phi_{ph}(\lambda)d\lambda \tag{2.16}$$

2.3.2 Intermediate Band Solar Cells

Intermediate band solar cells (IBSCs) have been proposed in an effort to improve a conversion efficiency of solar cells [2]. It is theoretically predicted that the introduction of an intermediate band allows two sub-bandgap carrier transitions, leading to increased photocurrent without output voltage degradation. Figure 2.14(a) shows a schematic band diagram of an IBSC with three quasi-Fermi levels of the valence band (ε_{FV}), intermediate band (ε_{IV}), and conduction band (ε_{CV}). When the energy gap between the valence band and intermediate band is ~0.7 eV, the conversion efficiency of an IBSC is the maximum of 63.1 % under full concentration as seen in Fig. 2.14(b). The maximum efficiency of an IBSC is much higher than that of a two-terminal ideal double-junction cell and single bandgap cell.

The first IBSC using multi-stack InAs quantum dots (QDs) has been developed [5]. As expected, the IBSC showed an extended external quantum efficiency (EQE) response in the near infrared wavelength region, as seen in Fig. 2.15(a). The current density-voltage characteristics of the IBSC and GaAs control cell without the QDs are shown in Fig. 2.15(b). The improved EQE of the IBSC contributed to the increased short-circuit current density. However, the open-circuit voltage was highly reduced, which is lower than that of a GaAs control cell. As a result, the conversion efficiency of the IBSC is lower as compared to that of a control cell. In addition, Blokhin *et al.* fabricated a quantum dot solar cell (QDSC) with InGaAs QDs, which were inserted in the intrinsic GaAs layer of a reference cell without the QDs (Fig. 2.16(a)) [31]. The conversion efficiency of the QDSC is lower than a reference cell due to the reduced open-circuit voltage, as shown in Fig. 2.16(b).

The poor device performance of the QD-based IBSCs is due to the introduction of InAs QDs in solar cell structures, which increases strain accumulation and decreases

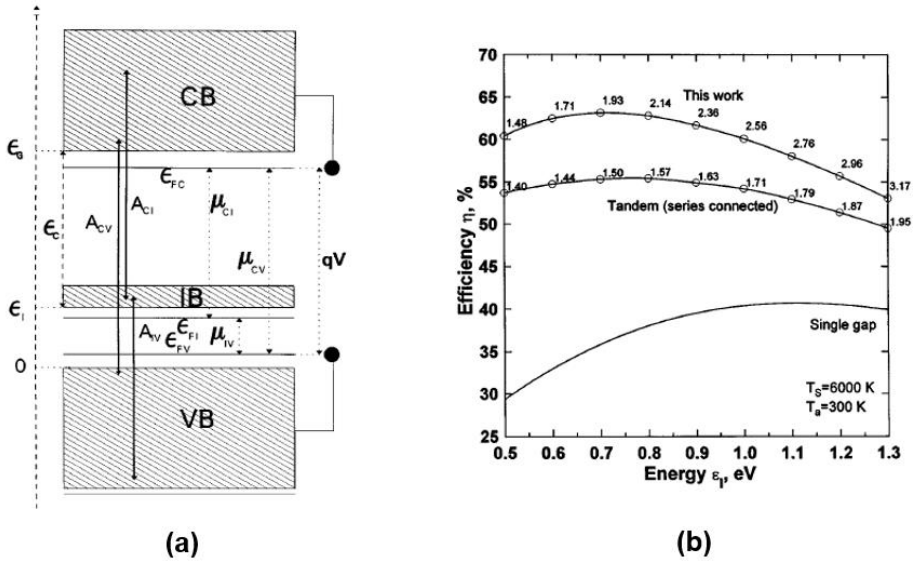

Fig. 2.14 (a) Band Diagram of an IBSC and (b) Detailed Balanced Efficiency Limit for an IBSC, Two-terminal Tandem, and Single Bandgap Cell [2]

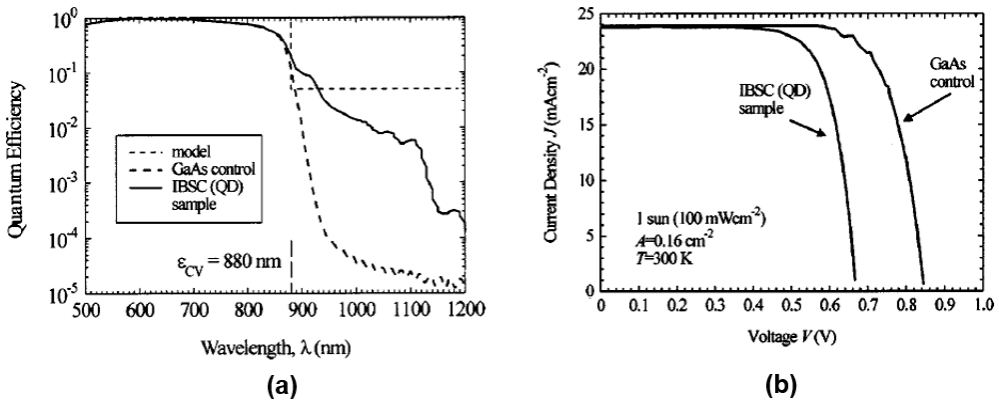

Fig. 2.15 (a) External Quantum Efficiency Spectra of the Fabricated IBSC and GaAs Control Cell and (b) Their Current Density-Voltage Characteristics under One-sun Illumination [5]

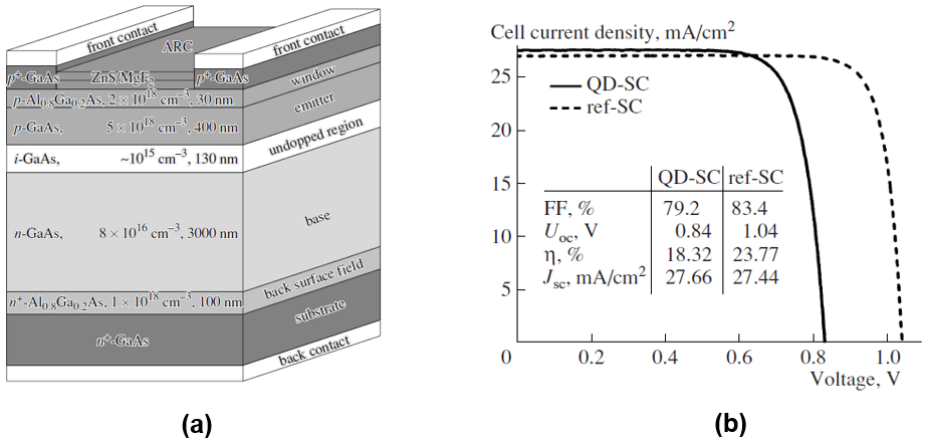

Fig. 2.16 (a) Schematic Structure of a GaAs Reference Cell and (b) Current Density-Voltage Characteristics of the Fabricated QDSC and Reference Cell under One-sun Illumination [31]

effective energy bandgap of host materials. Much effort has been done to reduce strain accumulation in InAs QDs to improve device performance of IBSCs using strain compensation layers such as GaP and GaNAs [32,33]. Hubbard *et al.* grew and characterized InAs/GaAs QDSCs with/without GaP layers [32]. As shown in Fig. 2.17(a), the QD stacks are embedded in the intrinsic region of the *p-i-n* solar cell structure. The introduction of GaP strain compensation layers improved the device performance, as seen in Fig. 2.17(b). However, the conversion efficiency of the QDSC with GaP layers was much lower than that of a baseline cell without the QDs owing to the highly degraded open-circuit voltage. Therefore, high-quality multi-stack InAs QD layers are required to be grown without significant output voltage degradation to improve the conversion efficiency of the QD-based IBSCs.

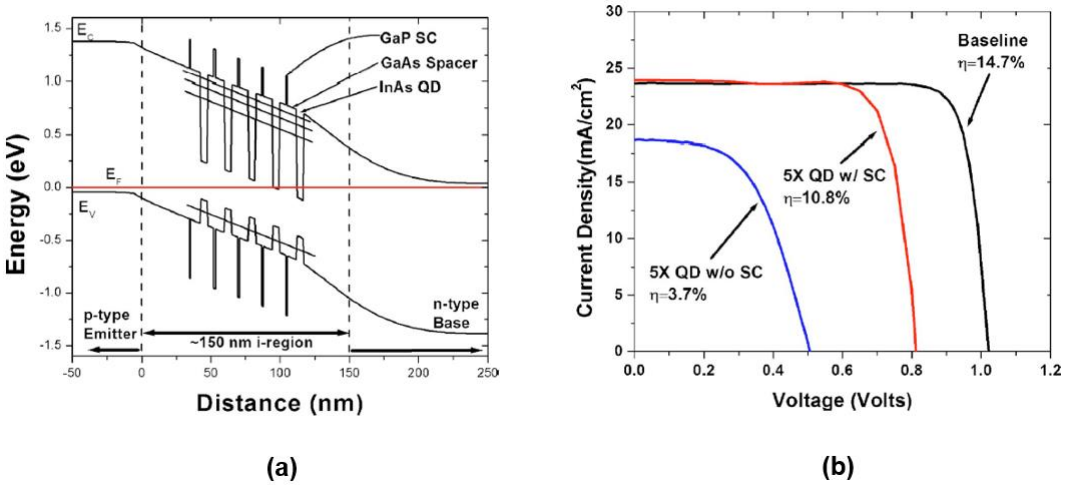

(a) (b)

Fig. 2.17 (a) Schematic Band Diagram of the QDSC with GaP Layers and (b) Current Density-Voltage Characteristics of the QDSCs with/without GaP Layers and a Baseline Cell [32]

2.4 Material and Device Characterization

2.4.1 Structural Characterization

Structural properties of as-grown structures are characterized using various techniques such as atomic force microscopy (AFM), x-ray diffraction (XRD), and transmission electron microscopy (TEM). The structural morphology and areal density of InAs QDs are evaluated by AFM whereas their strain and crystal quality are probed by XRD and TEM.

1) *AFM*: AFM measures surface features such as lateral dimension, height, and roughness of nanostructures with a sharp cantilever (Fig. 2.18). When a cantilever approaches sample surfaces it bends due to atomic repulsive and attractive interactions. A repulsive interaction between a cantilever and sample atoms is induced when the spatial distance between them is very close, while attractive interaction is caused by polarization interaction between sample atoms. The photodetector measures the deflection of a cantilever. The feedback loop plays a role of calibrating a relative distance between a cantilever and sample surface to make the frequency and phase constant. The piezoelectric scanner controls the sample positions with high accuracy and electrical signals are processed by a computer to acquire AFM images.

2) *XRD*: XRD is a widely used technique to study layer thickness, composition, strain, and crystalline defect density of epitaxial structures. As shown in Fig. 2.19(a), the periodic atomic planes with an interplanar spacing diffract incident x-ray beams. According to Bragg's law, the relation between interplanar spacing of crystal and diffraction angle is expressed as follows.

$$\lambda = 2d_{hkl}\sin\theta_B \tag{2.17}$$

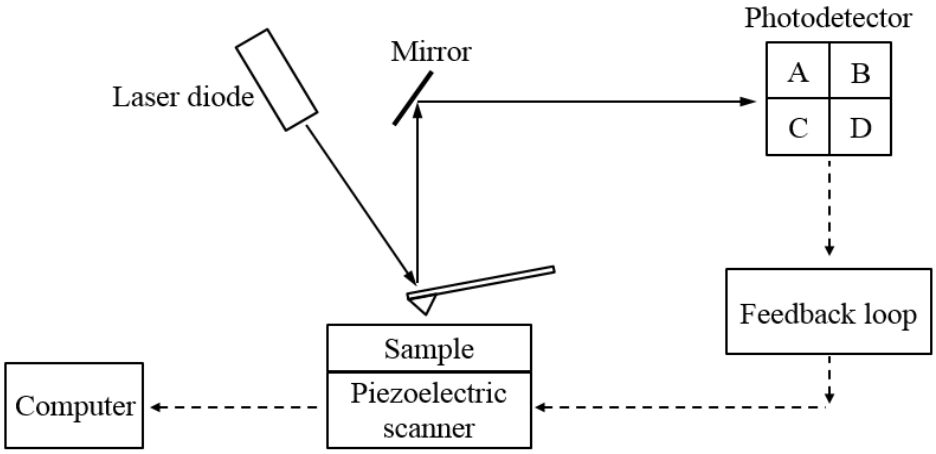

Fig. 2.18 Schematic of the Operation of Atomic Force Microscope

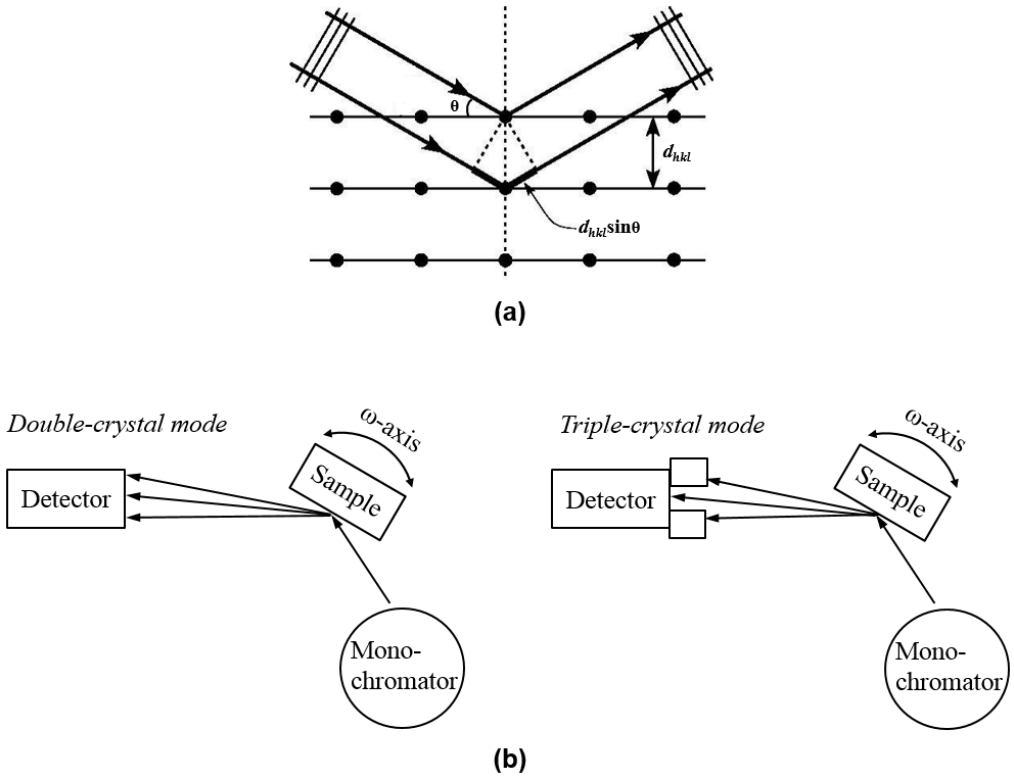

Fig. 2.19 (a) Schematic of X-ray Diffraction Showing the Path Difference between Adjacent X-rays of $2d_{hkl}\sin\theta$ (b) Schematic of Double-crystal and Triple-crystal XRD Modes

$$d_{hkl} = \frac{a_0}{\sqrt{h^2 + k^2 + l^2}} \tag{2.18}$$

where λ is the x-ray wavelength, d_{hkl} is the interplanar spacing of (*hkl*) planes for cubic systems, a_0 is the lattice constant of crystal, and θ_B is the diffraction angle. In our XRD measurements, we have used double-crystal and triple-crystal XRD modes as seen in Fig. 2.19(b). In the DC mode, all Bragg angles can be detected at the same time since the sample is rotated around ω-axis while only specific diffraction peak is measured due to the use of an analyzer in front of detector in the TC mode.

3) *TEM*: TEM uses a high voltage (50−400 kV) to accelerate electrons under vacuum. The electron wavelength (λ) of TEM and accelerating voltage (V) are correlated as follows.

$$\lambda = \frac{h}{\sqrt{2m_0 eV\left(\frac{1+eV}{2m_0c^2}\right)}} \tag{2.19}$$

where h is the Planck constant, m_0 is the electron mass, e is the electron charge, and c is the speed of light. Thus, the increase of accelerating voltage decreases the electron wavelength and thus increases TEM resolution. In Fig. 2.20, electron beams are focused by condenser lenses and transmitted through specimens. The transmitted electrons with information on sample structures are focused by objective lens and the magnified electron images are recorded by photographic films or CCD camera.

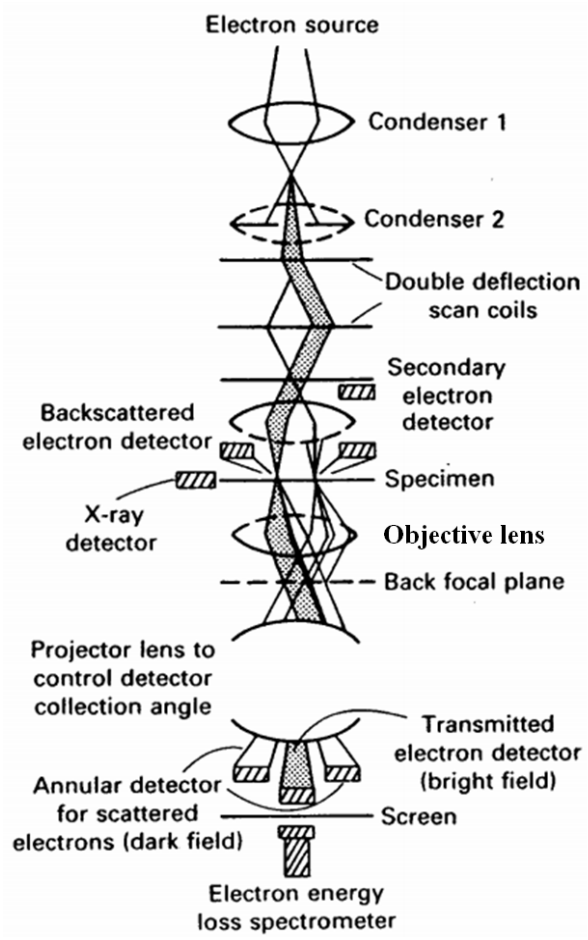

Fig. 2.20 Schematic Diagram of a Transmission Electron Microscope

2.4.2 Optical Characterizations

InAs QDs have peculiar optical properties such as emission wavelength tunability and high quantum yield, which originate from their zero-dimensional structures. Photoluminescence (PL) is a very effective and nondestructive technique to characterize optical properties of InAs QDs. In our work, we have used time-integrated PL and time-resolved PL to study interband optical transitions and carrier dynamics in the QDs, respectively.

1) *Time-integrated PL*: In time-integrated PL measurement, a laser light is chopped to high frequencies to increase signal-to-noise ratio and then excites QD samples in a cryostat, as shown in Fig. 2.21. After the optical excitation, electron-hole pairs are generated in barrier materials and then they are captured in QDs. Due to strong quantum confinement of QDs, most of the carriers confined in QDs radiatively recombine, leading to the emission of infrared photons. The emitted infrared photons are focused into the monochromator by a lens in front of a cryostat. The monochromator splits them into different photon energies and they are converted into electric signals by a photodiode. Finally, the detected signals are amplified by a lock-in amplifier and displayed in a computer.

2) *Time-resolved PL*: When QD samples are optically excited, the photogenerated electron-hole pairs go through carrier capture, relaxation, and recombination processes in QDs, which occur on an ultra short time scale. The time-resolved PL allows one to investigate such carrier dynamics since it uses a time-correlated single photon counting (TCSPC) system which detects single photons and measures their arrival times. Figure 2.22 shows schematic diagrams of a time-resolved PL system. The laser light is split in two by a beamsplitter. One of the laser light is incident on the sample surface, whereas the other goes through a fast photodiode

serving as a timing reference for the starting of the measurement. The emitted photons from the sample are sent to a monochromator and dispersed photon energies are detected by a photodiode. The discriminator removes timing jitters caused by a variation of electrical pulse height. The correlator generates output pulses from START and STOP measurement and they are recorded and displayed by a computer.

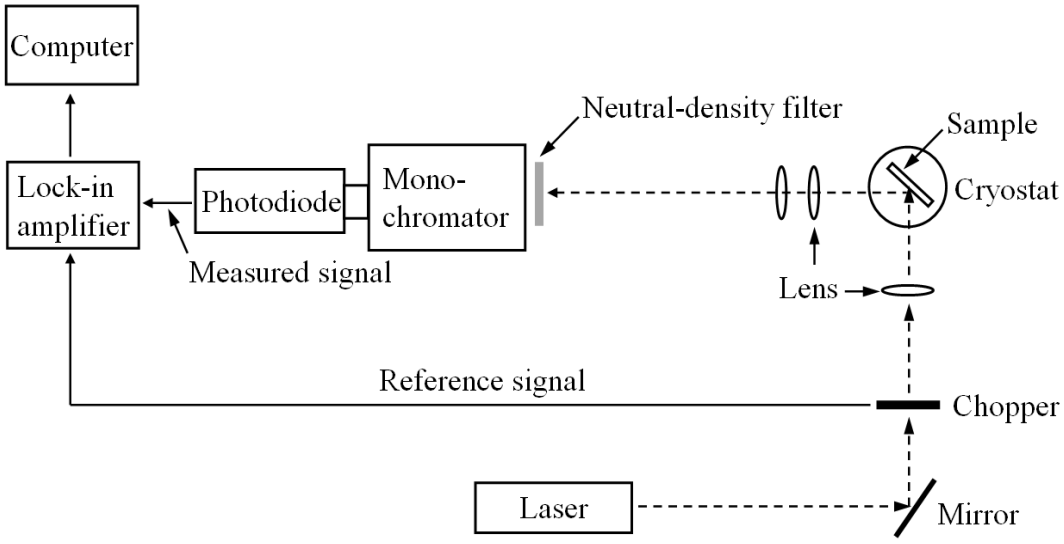

Fig. 2.21 Schematic Diagram of a Time-integrated Photoluminescence System

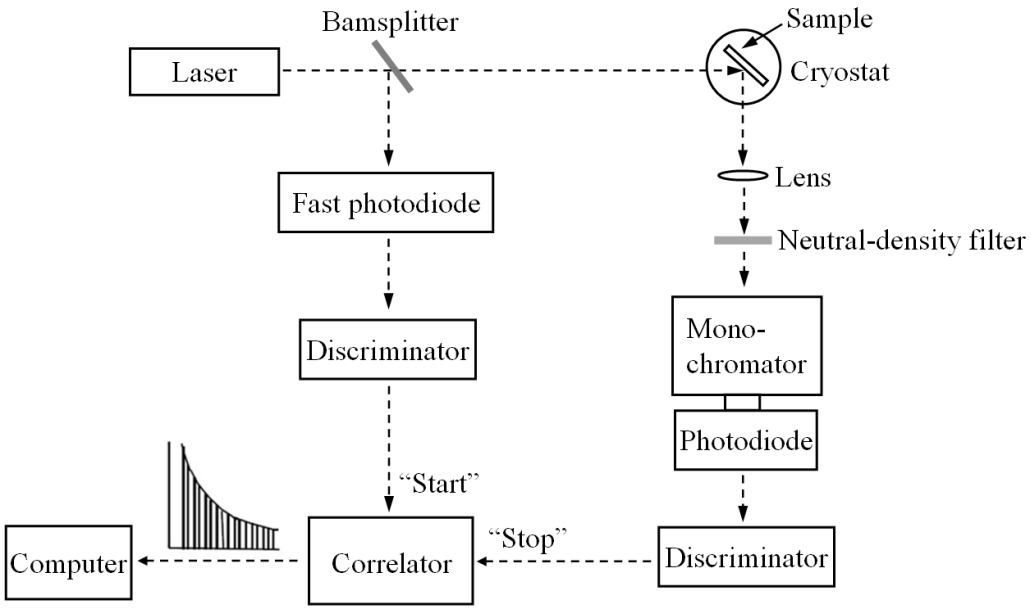

Fig. 2.22 Schematic Diagram of a Time-resolved Photoluminescence System

2.4.3 Electrical Characterizations

The electrical characteristics of fabricated solar cells are characterized with an external quantum efficiency (EQE) measurement equipment and solar simulator.

1) *EQE*: EQE is defined as the ratio of the number of electron-hole pairs externally created by the solar cell to the number of incident photons on the solar cell. The optical loss and bulk/surface recombination of solar cells cause the degradation in EQE. The optical loss can be reduced by using antireflection coating and optimizing finger layouts, while the front surface recombination can be suppressed by surface passivation.

2) *Solar simulator*: The device parameters of fabricated solar cells are measured by a solar simulator under one-sun intensity (100 mW/cm^2) at AM 1.5G. Figure 2.23(a) shows a schematic setup of a solar simulator. The solar simulator uses a Xenon lamp to emit white light. The white light is reflected by a primary mirror and filtered through an AM 1.5G filter to simulate the solar spectrum at AM 1.5G (Fig. 2.23(b)). Then, the simulated light beam passes through a collimating lens in order to reduce incident beam angle and thus to collimate the beam. Finally, the collimated beam is incident on the solar cell.

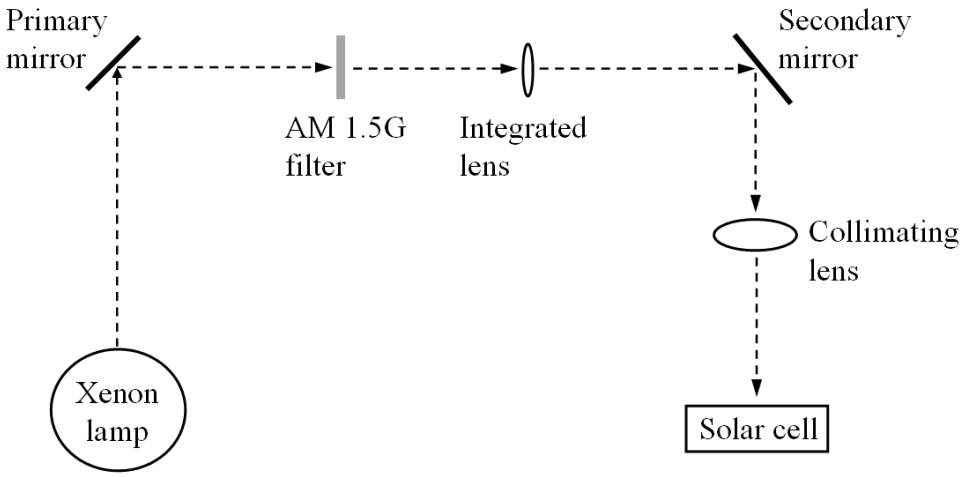

(a)

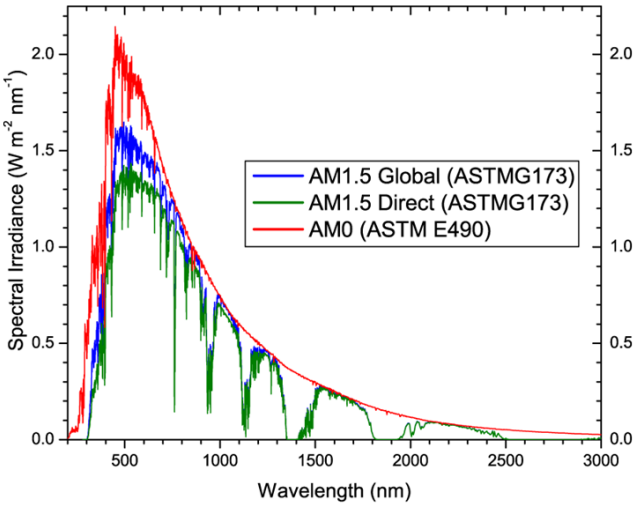

(b)

Fig. 2.23 (a) Schematic Setup of a Solar Simulator and (b) Standard Solar Spectra from the American Society for Testing and Materials

Chapter 3

EFFECT OF SILICON DELTA-DOPING DENSITY ON OPTICAL PROPERTIES OF TYPE-II INAS/GAASSB QUANTUM DOTS

3.1 Introduction

Semiconductor quantum dots (QDs) have been extensively studied over the last decades for optoelectronic devices such as QD laser diodes [34], QD infrared photodetectors (QDIPs) [35], and intermediate band solar cells (IBSCs) [2,4] because of their strong carrier confinement and delta-function-like density of states. In IBSC applications, the introduction of QDs enables solar cells to absorb sub-bandgap photons, leading to photocurrent improvement. In particular, InAs/GaAs QDs have been extensively studied to increase conversion efficiency of IBSCs beyond that of a control cell without QDs. However, the conversion efficiency of InAs/GaAs QD-based IBSCs has been lower compared to that of their control cells. Recently, InAs/GaAsSb QDs have been recently suggested as a promising material candidate owing to their structural advantages over the InAs/GaAs QDs for improving the device performances of QD-based IBSCs. Unlike InAs/GaAsQDs with a large valence band offset (VBO), the VBO of InAs/GaAsSb QDs can be calibrated by varying Sb compositions [36]. The QD structures with a negligible VBO are predicted to have an improved open-circuit voltage (V_{oc}) which is unobtainable from the InAs/GaAs QD based IBSCs [8]. Moreover, the carrier lifetime in the QDs can be prolonged by increasing Sb composition, resulting from the change in the energy band alignment from type-I to type-II structure [10]. Along with these advantages, as the intermediate band is half-filled with electrons, the short-circuit current density (J_{sc}) of the IBSCs will be increased due to the absorption of the subband gap photon energies [4]. To do this, the silicon (Si) delta (δ)-doping can be employed as an effective way to fill the electronic states of QDs

with electrons because of its high electron-injection efficiency [37]. When Si δ-doping is introduced in a barrier layer such as GaAs(Sb), electrons confined in a δ-doped potential well are thermally activated and/or tunnel through the barrier and they are captured by InAs QDs. As a result, the number of electrons populated in the QDs increases with increasing the doping density. Despite such importance, the optical properties of Si δ-doped type-II InAs/GaAsSb QDs have not been sufficiently addressed [35,36].

In this chapter, we report on the optical properties of type-II InAs QDs embedded in GaAsSb layers with different Si δ-doping densities. We find that the blueshift rate of the ground state (GS) emission under increasing photoexcitation becomes slower with increasing the doping density. The increase in the relative PL intensity of the GS emission to the first excited state (ES) emission with the doping density indicates that the radiative recombination rate at the GS subband levels is faster with increasing the doping density. In addition, the doping density affects the redshift rate of the GS emissions with increasing temperature. Further, time- resolved PL reveals that the total radiative lifetime of the lightly doped QD sample (5×10^{10} cm^{-2}) becomes longer than that of the undoped sample. When the doping density increases up to (2×10^{12} cm^{-2}) the radiative lifetime is shorter through the enhanced radiative recombination.

3.2 Experimental Procedure

All samples were grown by a solid-source molecular beam epitaxy (MBE) system. After the thermal deoxidation at 580℃, a GaAs buffer layer of 400 nm was grown at 600℃ on a semi-insulating GaAs (001) substrate as shown in Fig. 3.1. Then, the substrate temperature was ramped down to 500℃. At the lowered substrate temperature, a 10 nm-thick GaAsSb barrier with Sb to As flux ratio of 0.03 was grown and then an InAs layer with a nominal coverage of 2 monolayers (MLs) was grown at a growth rate of 0.04 ML/s, followed by growing a 10 nm-thick GaAsSb barrier. During the growth of the GaAsSb barrier, Si δ-doping was performed 2 nm below the InAs QD layer with areal doping densities of 5×10^{10}, 5×10^{11}, and 2×10^{12} cm^{-2}. The QD structures were finally capped with a 200 nm-thick GaAs layer at 600℃ for continuous-wave (cw) and time-resolved photoluminescence (TRPL) studies. As a reference sample, an undoped sample without Si δ-doping was also grown under the same growth conditions. The Sb composition of GaAsSb was determined to be 17 % by double crystal ω–2θ x-ray diffraction measurements, and thus the as-grown samples in this study have type-II energy band alignments.

To examine the optical properties of the QD samples, we utilized a Nd:YAG laser (λ = 532 nm) and a liquid nitrogen cooled InGaAs photodetector for cw-PL measurements, and a time-correlated single photon counting (TCSPC) system with a 200 fs Ti:Sapphire laser (λ = 800 nm) with a repetition rate of 250 kHz to measure the decay transients of the QD emissions at 4.2 K for TRPL measurements. The penetration depth of the lasers for cw-PL and TRPL system exceeded the epilayer thickness of the QD samples and hence the carrier injection level by the optical pumping was expected to remain same for cw-PL and TRPL measurements in order to consistently characterize PL emission wavelength and carrier lifetime for the QD samples.

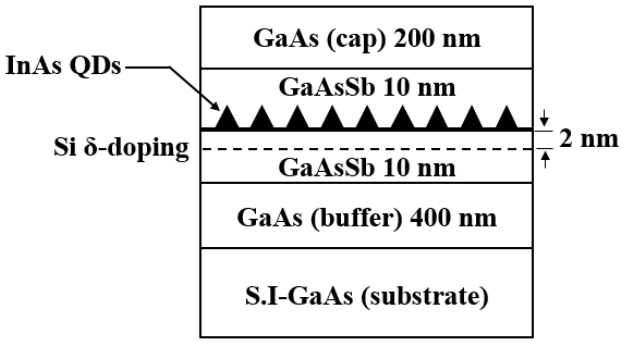

Fig. 3.1 Schematic Sample Structure of Type-II InAs/$GaAs_{0.83}Sb_{0.17}$ QDs with Different Si δ-doping Densities of 5×10^{10}, 5×10^{11}, and 2×10^{12} cm^{-2}

3.3 Results and Discussions

Excitation power dependent PL measurements at 10 K were conducted to identify the band alignments of the InAs/GaAsSb QDs. The PL peak energies of the GS emissions of the all QD samples linearly increase with the cube root of the excitation power as shown in Fig. 3.2. The GS emission peaks of the samples A, B, C, and D experience the blueshifts of 28, 35, 17, and 7 meV, respectively. The PL blueshift is observed in the quantum structures with a type-II band alignment due to the spatial separation of electrons and holes where as it does not occur in type-I quantum structures [38,39]. The large blueshift of 35 meV for the sample B originates from a strong band bending effect caused by the electron injection into the QDs. As more electrons are confined in QDs, the attractive Coulombic interactions between electrons confined in QDs and holes localized in GaAsSb layers increase, and thus strengthen the internal electric fields at the interface as seen in Fig. 3.3. The enhanced electric field causes more band bending, giving rise to a stronger blueshift in the PL spectrum. On the other hand, the blueshift rate of the GS emission peak is slower with increasing the doping density up to 2×10^{12} cm^{-2}. This phenomenon can be explained as follows. The spatially separated carriers produce a triangular potential well with an electric field intensity of [40]

$$F = \frac{2\pi en}{\varepsilon_0} \propto \left(\frac{P}{\gamma}\right)^{1/2} \tag{3.1}$$

where n, P, and γ are the photoexcited electron density in the GaAs and GaAsSb barrier layers, excitation power density, and radiative recombination rate, respectively. Further, the GS energy shift by the electric field is given by the following equation:

$$\Delta E_C \propto F^{2/3} \propto \left(\frac{P}{\gamma}\right)^{1/3} \tag{3.2}$$

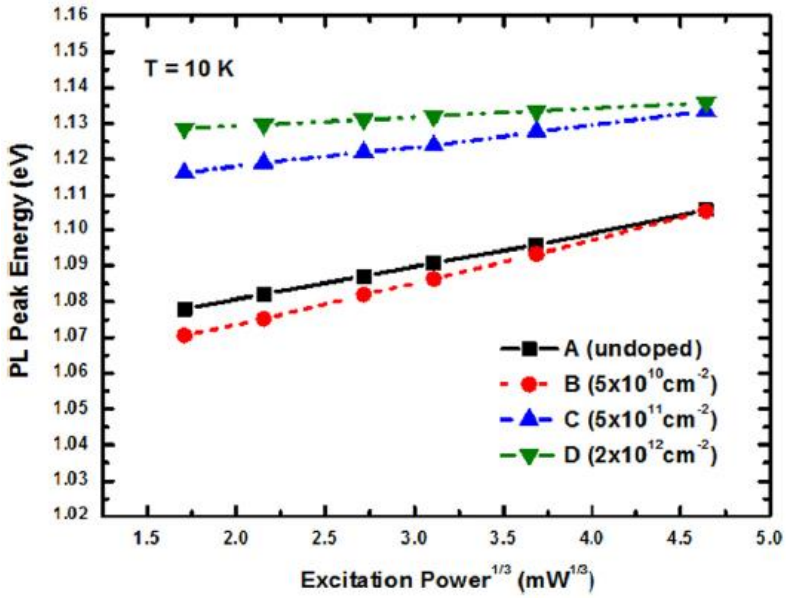

Fig. 3.2 GS PL Peak Energy Shift against the Cube Root of the Excitation Power for the QD Samples at 10 K. The Lines are Least-squares Fits for the Experimental Data Points

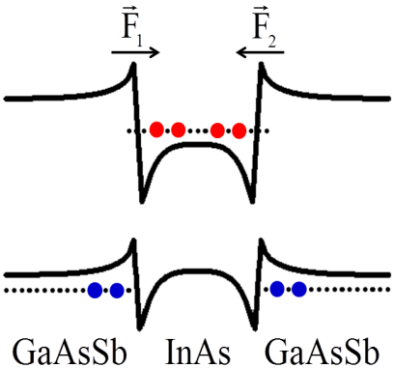

Fig. 3.3 Schematic Band Structure of Type-II InAs/GaAsSb Heterojunction where the Internal Electric Fields $F_{1(2)}$ are Induced by the Band Bending Effect

From Eq. (3.2), we note that the GS energy shift is inversely proportional to the cube root of the radiative recombination rate (γ). As shown in Fig. 3.2, the blue shift rate slows down as the doping level increases. This is attributed to the more electrons in the QDs injected from the δ-doped plane since they induce the carrier-carrier scattering and, in turn, the fast carrier relaxation in the QD region. This results in the increased radiative recombination rate due to enhanced Coulombic interaction between built-in electrons and optically injected holes under the photoexcitation [41]. Since the doping level of the sample B is comparable with a QD number density of 5×10^{10}, only one electron can preoccupy QD electronic levels. Thus, the carrier-carrier scattering inducing the fast radiative recombination rate could be not pronounced to expedite the radiative recombination rate in the sample B.

Figure 3.4 exhibits the PL spectra separated by multiple Gaussian peaks at 10 K using an excitation power of 100 mW to observe the QD emissions from higher ES transitions. The GS PL peaks are centered at 1.103 eV and 1.105 eV corresponding to the E_0H_0 transitions for the samples A and B, respectively. In addition, two ES peaks of 1.138/1.129 eV and 1.158/1.157 eV are observed corresponding to the E_1H_0 and E_1H_1 transitions for the samples A and B, respectively. These interband optical transitions are in a good agreement with our previous report [10]. The PL intensity ratio of E_0H_0 to E_1H_0 goes up with the doping density. This implies that the GS radiative recombination is enhanced by the Coulombic interaction across the InAs/GaAsSb interface as the doping level increases. Interestingly, while the increase of the PL intensity ratio is not significant for the sample it turns out to be much pronounced in the case of the samples C and D. This trend is taken as evidence that the fast relaxation induced by the δ-doping takes much more effect when the QD electronic levels are fully occupied. Compared to the samples A and B, the GS peak of

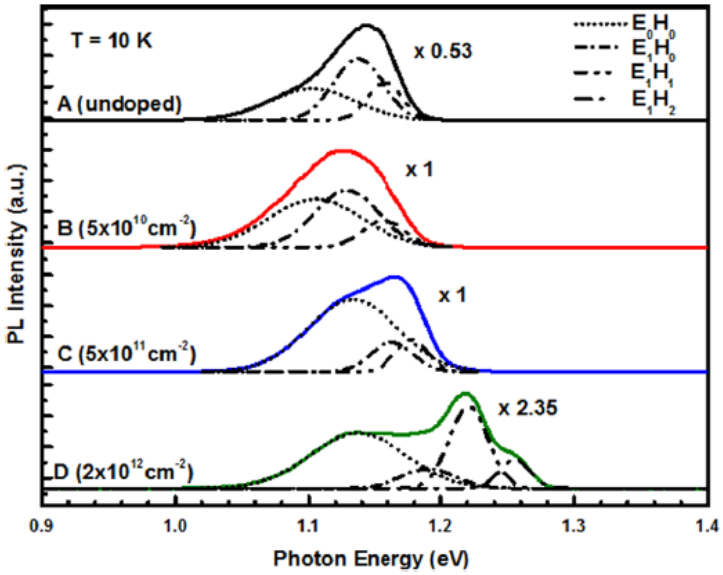

Fig. 3.4 PL Spectra at 10 K at an Excitation Power of 100 mW. Each PL Spectrum was Decomposed into Gaussian Functions Showing Interband Transitions. (E_0, E_1: Electron Ground and First Excited State/H_0, H_1, H_2: Hole Ground, First, and Second Excited State)

the samples C and D is blueshifted by ~33 meV. This trend is consistent with the report that the PL emission of GS transition for Si doped InAs/GaAsSb QDs and InAs/GaAsQDs was blueshifted by ~80 meV as compared to the undoped QD sample [37]. This large blueshift of the GS peak emission is likely due to the state filling effect in the QDs [42]. The nonparity transitions such as E_1H_0 and E_1H_2 where the selection rule is absent are observed due to the spatial separation of carriers in the type-II QD structure [10].

The temperature dependent behaviors of the GS peaks of the QD samples are displayed in Fig. 3.5. The GS peak energy decreases with increasing temperature due to the carrier redistribution in the QDs through the interdot hopping process from smaller QDs to larger ones with temperature [10] as seen in Fig. 3.6. In order to evaluate the redshift rate as a function of temperature, the PL peak energies are fitted using the empirical Varshni relation [43]. The redshift rates within the investigated temperature range from 10 K to 300 K are determined to be 0.30, 0.36, 0.48, and 0.28 meV/K for the samples A, B, C, and D, respectively. The redshift rates of the InAs QDs are higher compared to that of 0.25 meV/K of an InAs bulk. The redshift rates of all QD samples are comparable in the low temperature region (< 130 K) while the difference in the redshift rate becomes more prominent in the high temperature region (> 130K). The redshift rate is faster with the doping density up to 5×10^{11} cm^{-2} and decreases at a doping density of 2×10^{12} cm^{-2}. As the temperature increases, more electrons in the δ-doped plane are thermally activated and captured in the QDs, forming positively charged Si donors. The localized electric fields coming from the ionized donors are calculated to be 6.8, 67.2, and 268.8 kV/cm for the samples B, C, and D, respectively [44]. These electric fields can redshift the interband transition energy E which is known as quantum confined Stark effect following a quadratic dependence on the field F [45],

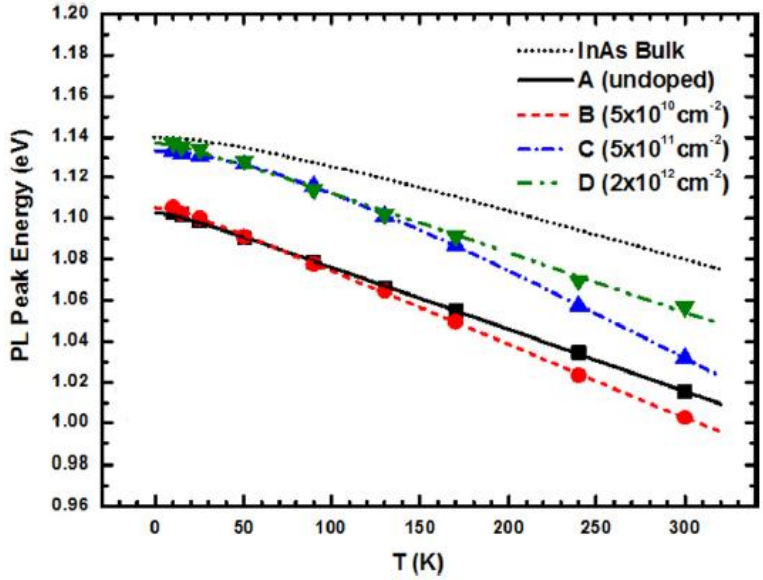

Fig. 3.5 Temperature Dependence of the GS Peak Energies of All QD Samples (The Data Points are Fitted using the Varshni Law)

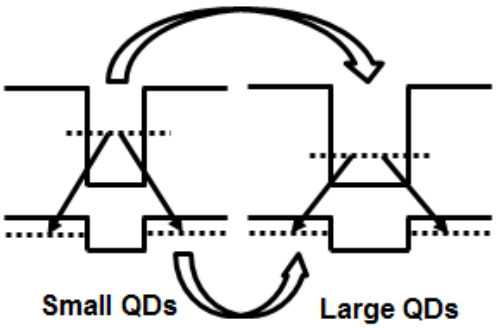

Fig. 3.6 Interdot Hopping Process where Carriers Jump from Small QDs to Large QDs with Increasing Temperature

$$E = E_o + \alpha F + \beta F^2 \tag{3.3}$$

where E_0, α, and β are the transition energy at F = 0, permanent dipole moment, and polarization in the direction of the electric field, respectively. Accordingly, the redshift is expected to be more pronounced with increasing the doping density. The decrease in the redshift rate of the sample D, despite the highest doping density, is ascribed to the improved QD size uniformity as a result of the suppression of QD coalescence by the doping [46].

In order to study the effect of the doping density on the carrier lifetime in the QDs, TRPL measurements were carried out at 4.2 K. It was known that the type-II InAs/GaAsSb QDs show the biexponential decay traces with a fast decay component and slow decay one [47]. The TRPL decay transients, as shown in Fig. 3.7, of the GS peaks are fitted by the biexponential decay function:

$$I(t) = A_1 \exp(-t/\tau_1) + A_2 \exp(-t/\tau_2) \tag{3.4}$$

where I is the integrated PL intensity, $A_{1(2)}$ is the fitting constant, and $\tau_{1(2)}$ is the carrier lifetime. The short carrier lifetime τ_1 results from the short-range radiative recombination of the carriers near the heterointerface at the initial decay stage. As the spatially separated carriers are more recombined, the band bending effect is reduced, weakening the wavefunction overlap of elections and holes. As a result, the reduction of recombination probability of the carriers gives rise to a long-range radiative lifetime τ_2. As listed in Table 3.1, the τ_1 at the initial recombination stage becomes shorter with increasing the doping density. After the initial recombination, the τ_2 increases with the doping density up to 5×10^{10} cm^{-2}. However, a further increase in the doping density results in the decrease of the τ_2. This carrier lifetime dependence on the doping density is in accordance with the tendency showing that the radiative recombination rate increases with the doping density as stressed in Fig. 3.2.

A possible mechanism from the TRPL data taken here is as follow. The electrons from the δ-doped plane preoccupy the QD electron subband levels. When the δ-doping level of 5×10^{10} cm^{-2} is used beneath the QD plane the QD electron GS is half-filled. Since the electrons and holes are spatially separated in the QD structure, the carrier-carrier scattering in the type-II structure may not occur as much as type-I structures when the δ-doping is utilized as an electron supply. Therefore, the half-filled QD electron GS could be not enough to introduce a significant carrier-carrier scattering that results in the carrier relaxation and, in turn, electron-hole recombination in the QDs. As seen in Fig. 3.7, the sample B (5×10^{10} cm^{-2}) has a longer total radiative recombination time compared to the sample A (undoped). It is because the fast carrier relaxation by carrier-carrier scattering in the QD region is not induced when the QD electronic levels are lightly filled. Nevertheless, when the doping level is increased up to 2×10^{12} cm^{-2} the QD electronic levels are fully occupied. This causes the fast carrier relaxation in the QDs and enhanced radiative recombination [48] leading to the creation of a strong band bending across the interface between InAs and GaAsSb as explained in Fig. 3.2. When considering the application of the δ-doped QDs to IBSCs, the long carrier lifetime in the QDs is needed to improve the photogenerated charge collection which is a key parameter affecting the efficiency of the QD-based IBSCs [49,50]. We note that the type-II QDs with optimized doping density have a potential for the realization of the high-efficiency IBSCs owing to the increased carrier lifetime.

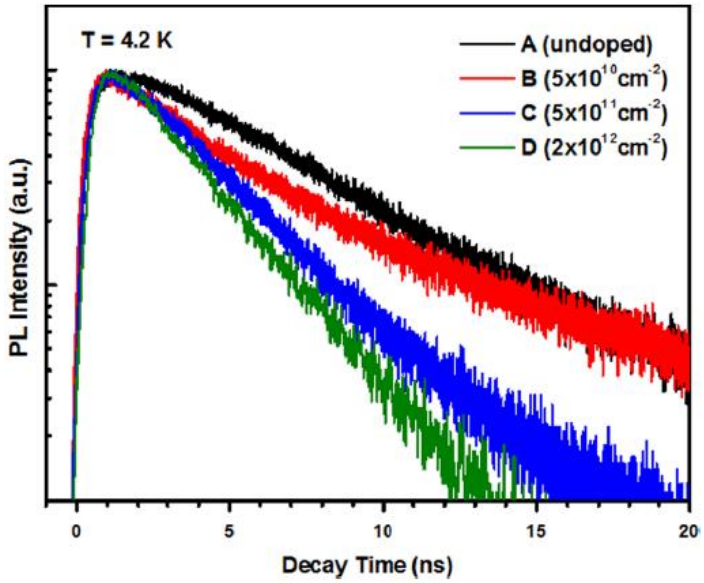

Fig. 3.7 TRPL Decay Transients of the GS Peaks for the InAs/$GaAs_{0.83}Sb_{0.17}$ QDs at 4.2 K

Sample	τ_1 (ns)	τ_2 (ns)
A (undoped)	4.2	8.3
B ($5x10^{10}cm^{-2}$)	2.6	10.2
C ($5x10^{11}cm^{-2}$)	2.3	5.2
D ($2x10^{12}cm^{-2}$)	1.6	2.9

Table 3.1 Carrier Lifetimes, $\tau_{1(2)}$, of the QD Samples Determined from the Biexponential Fitting

3.4 Conclusion

In conclusion, we have studied the optical properties of Si δ-doped type-II InAs/GaAsSb QDs. At the low temperature of 10 K, the increased electron population in the QDs by the δ-doping slows down the PL blueshift rate by the enhanced carrier-carrier scattering, and increases the PL intensity ratio of the GS emission to the first ES emission, indicating the faster radiative recombination at the GS subbands. Further, the redshift rate of the GS emissions with temperature (> 130 K) is accelerated with the doping density up to 5×10^{11} cm^{-2} and drops down at a further increased doping density of 2×10^{12} cm^{-2}. From TRPL measurement, it is demonstrated that the total radiative lifetime is extended when the δ-doping level of 5×10^{10} cm^{-2} is used. However, when the δ-doping density increases up to 2×10^{12} cm^{-2} the total radiative lifetime decreases due to the enhancement of the radiative recombination induced by the fast carrier relaxation. The total radiative lifetime of the QDs is highly influenced by the QD electronic subband occupation which is controllable by calibrating the δ-doping levels.

The trends of the optical properties of InAs/GaAsSb QDs observed at low temperatures will translate for IBSCs operating at higher temperatures. This is because the extent of the electron injection from the δ-doped plane to the QD plane remains similar at high temperatures due to the high electron injection efficiency through the thermal excitation of electrons out of the δ-doped plane and/or direct tunneling to the QD plane. Thus, the built-in electrons by the δ-doping in QD electronic levels will induce the same doping effects at room temperature as they did at low temperatures.

Our findings suggest that the Si δ-doping in type-II InAs/GaAsSb QDs is an effective method to fill the subband levels of the QDs with electrons and to tune both the interband carrier transitions and carrier lifetimes, which are the highly required features to improve the IBSC performances.

Chapter 4

STRUCTURAL AND OPTICAL PROPERTIES OF SINGLE- AND MULTI-STACK INAS/GAASSB QUANTUM DOTS

4.1 Introduction

Self-assembled quantum dots (QDs) grown by Stranski–Krastanov growth mode have stimulated much interest in QD-based optoelectronic devices such as lasers and infrared (IR) photodetectors due to their peculiar electronic properties of discrete energy levels and three-dimensional carrier confinement [51,52].

In recent decades, third generation solar cells such as QD-based intermediate band solar cells (IBSCs) have been researched widely, aiming to exceed the Shockley-Queisser efficiency limit by absorbing the sub-bandgap photons [4]. It was reported that the short-circuit current density (J_{sc}) of the IBSCs was improved by the extended photon absorption in near-IR wavelength regions whereas the open-circuit voltage (V_{oc}) was severely degraded by the incorporation of the InAs QDs with a narrow bandgap. The QDs have the inherent structural drawbacks such as the nonuniform QD size distribution and large valence band offset (VBO) at the interface of InAs/GaAs inducing a V_{oc} loss [53,54]. To overcome such limitations of the InAs/GaAs QDs, InAs/GaAsSb QD systems have been identified as a promising material candidate [9,10]. They have several advantages over the InAs/GaAs QDs for IBSC applications as follows. The Sb acts as a surfactant which reduces the surface free energy, suppressing the coalescence of neighboring QDs. Accordingly, the incorporation of Sb composition improves the size uniformity of the QDs. Moreover, the VBO of the heterointerface of InAs/GaAsSb with an Sb composition of ~14 % is calculated to be negligible by eight-band $\boldsymbol{k \cdot p}$ theory. The V_{oc} loss, one of the most challenging issues of QD-based IBSCs, can be highly decreased by a negligible VBO of the QDs. Further,

the carrier lifetime improves with increasing an Sb composition because of the transformation of energy band alignment from a type-I to type-II structure.

In this chapter, we have studied the structural and optical properties of the single- and multi-stack InAs/GaAsSb QDs with different Sb compositions. A slight change in QD morphology is observed for the single-stack QDs. On the other hand, for the multi-stack QDs the QD size is changed with Sb composition. In addition, the increase of lattice mismatch between GaAs and GaAsSb causes larger strain relaxation of GaAsSb layers with increasing Sb composition. Along with these structural changes, interband optical transition and carrier lifetime in the QDs are found to change with Sb composition.

4.2 Experimental Procedure

Figure 4.1 shows the schematic structures of single- and multi-stack InAs/GaAsSb QDs. The single-stack QD structures with different Sb compositions were grown on semi-insulating GaAs (001) substrates by solid-source molecular beam epitaxy (MBE) system. A 400 nm-thick GaAs buffer layer was grown on the substrate at 580℃ after thermal cleaning of oxides on the substrate surface. To grow InAs/GaAsSb layers, the substrate temperature was lowered to 500℃ and a 10 nm-thick GaAsSb layer was grown. Then, 2 ML of InAs was deposited on the GaAsSb with a deposition rate of 0.04 ML/s. During the InAs deposition, reflection high-energy electron diffraction (RHEED) displayed chevron RHEED patterns, which is indicative of the formation of three-dimensional InAs QDs. The QDs were capped with a 10 nm-thick GaAsSb layer. The lower GaAsSb layer, located below InAs layers, was delta-doped with silicon at 2×10^{12} cm^{-2}. A 200 nm-thick GaAs layer was finally grown on the InAs/GaAsSb QD structure at 580℃. For the growth of multi-stack InAs/GaAsSb QDs, a silicon-doped n-GaAs buffer layer (300 nm) was grown at 580℃ and the substrate temperature was then lowered to 500℃ for the growth of InAs/GaAsSb QD stacks. At the lowered temperature, ten-stack InAs/GaAsSb layers consisting of 2 ML-thick InAs layer embedded in 10 nm-thick $GaAs_{1-x}Sb_x$ layers were grown. To calibrate Sb composition of GaAsSb layers, Sb to As flux ratios were varied to be 0.011, 0.021, and 0.028. In order to improve QD size uniformity, InAs layers were deposited at a slow growth rate of 0.04 ML/s and a growth interruption of 10 s under an As-rich condition was introduced after InAs QD formation which was monitored through RHEED by observing a transition from streaky to chevron patterns. The substrate temperature was then ramped up to 600℃ and an n-GaAs cap layer (300 nm) was grown on the ten-stack QD layers. The QD samples with Sb to As flux ratios of 0.011, 0.021,

and 0.028 are referred to as the samples A, B, and C, respectively. From the double crystal x-ray diffraction measurement, the Sb compositions of GaAsSb layers were determined to be ~7.3 %, ~9.8 %, and ~10.2 % for the samples A, B, and C, respectively.

For structural characterization, high-resolution transmission electron microscopy (TEM) measurements were performed using JEOL-2010F/JEOL-JEM 4000EX by Dr. Dinghao Tang at Arizona State University. In addition, high-resolution x-ray diffraction (XRD) measurements were conducted using X'Pert XRD diffractometer with $CuK_{\alpha 1}$ radiation (λ = 1.5406 Å). For optical characterization, continuous-wave photoluminescence (PL) system with a Nd:YAG laser (λ = 532 nm) and a cooled InGaAs photodiode was employed. In addition, a time-correlated single-photon-counting system with a Ti:Sapphire laser (λ = 800 nm) was used to observe PL decay of QD emissions for time-resolved PL measurement.

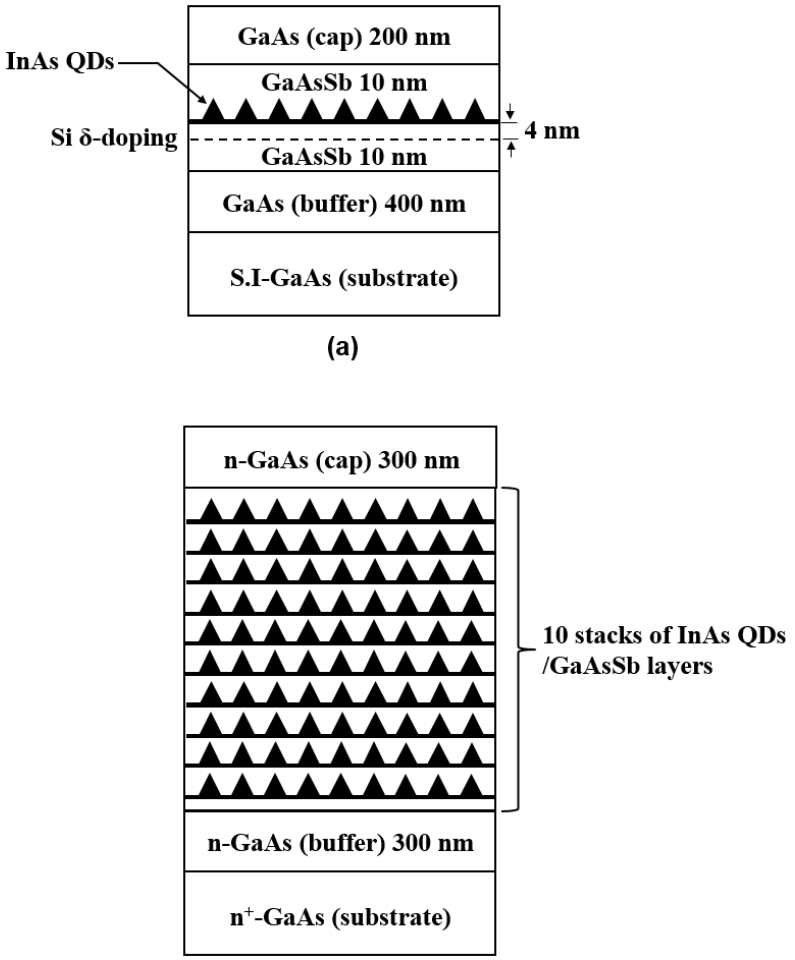

Fig. 4.1 Schematic Sample Structures of (a) Single- and (b) Multi-stack InAs/GaAsSb QDs with Different Sb Compositions

4.3 Results and Discussions

Figure 4.2 shows the high-angle annular dark-field (HAADF) scanning transmission electron microscopy (STEM) images of the single-stack InAs/GaAsSb QDs with different Sb compositions. Compared to the QDs (Sb 8 %), the aspect ratio, dot height/diameter, of the QDs (Sb 20 %) is higher. This is because the improved strain reducing effect with increasing Sb composition suppresses the QD decomposition and thus preserves a high aspect ratio of dots [55,56]. It is noted that the upper heterointerface between GaAs and GaAsSb of the QDs (Sb 8 %) is much sharper than that of the QDs (Sb 20 %) due to the reduced lattice mismatch strain at the interface with decreasing Sb composition. Figure 4.3 exhibits the HAADF-STEM images of the 10-stack InAs/GaAsSb QDs with varying Sb compositions. It is clearly observed that each QD layer is vertically aligned along the growth direction since the vertical QD stacking probability is nearly unity due to the strain field of underlying QD layer grown on a thin spacer layer with a thickness less than ~15 nm [57]. Another peculiarity of the HAADF-STEM images is that as the Sb composition of GaAsSb spacer layers increases, the QD areal density increases and QD height decreases. This is ascribed to the lowered critical thickness for the QD formation and the underlying strain field in the GaAsSb spacer, suppressing interactions between the adjacent QDs [9].

To estimate the relaxation of initial elastic stress of GaAsSb layers, the reciprocal space maps (RSMs) in the vicinity of the asymmetrical (224) reflections for the QD structures are scanned, as seen in Fig. 4.4. As Sb composition increases, the ΔQ_x between the GaAs and GaAsSb diffraction peaks increases in the RSMs. From the ΔQ_x, the strain relaxations of GaAsSb layers are evaluated to be 0, 18, and 23 % for the samples A, B, and C, respectively. The GaAsSb layers with higher Sb composition are more in-plane compressive-strained by

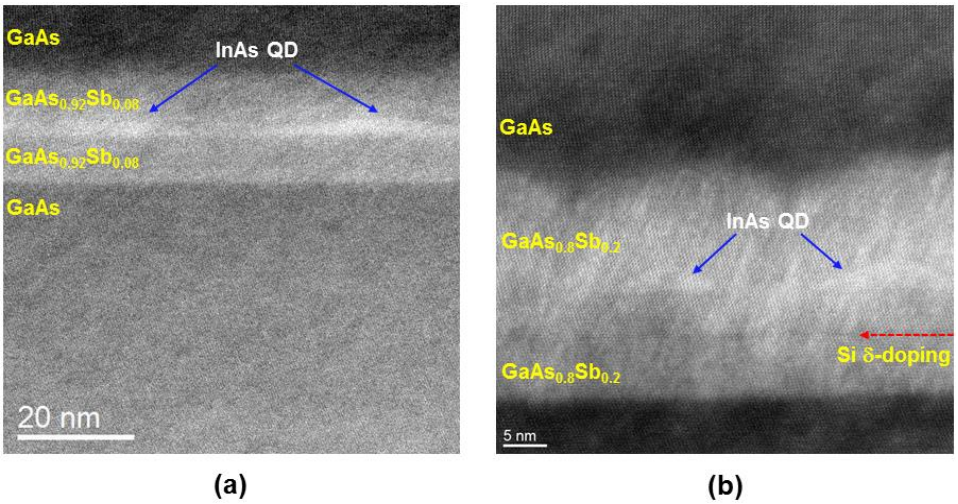

Fig. 4.2 HAADF-STEM Micrographs of the Single-stack InAs/GaAsSb QDs with Different Sb Compositions of (a) 8 % and (b) 20 %

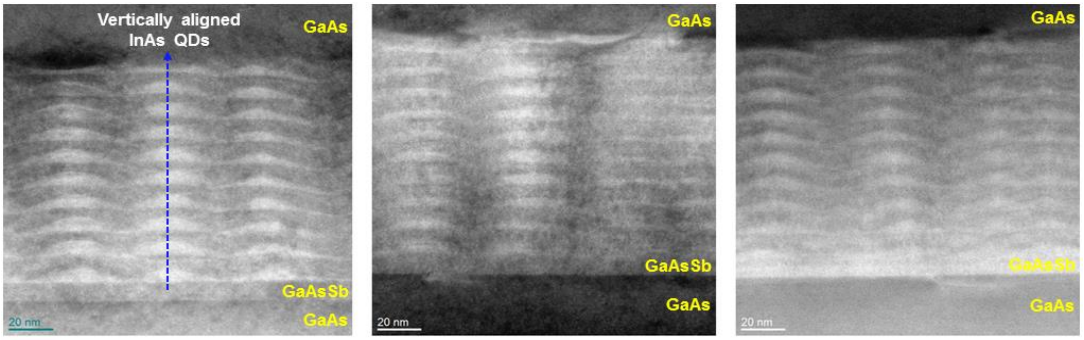

Fig. 4.3 HAADF-STEM Micrographs of the 10-stack InAs/GaAsSb QDs with Different Sb Compositions of (a) 7.3 %, (b) 9.8 %, and (c) 10.2 %

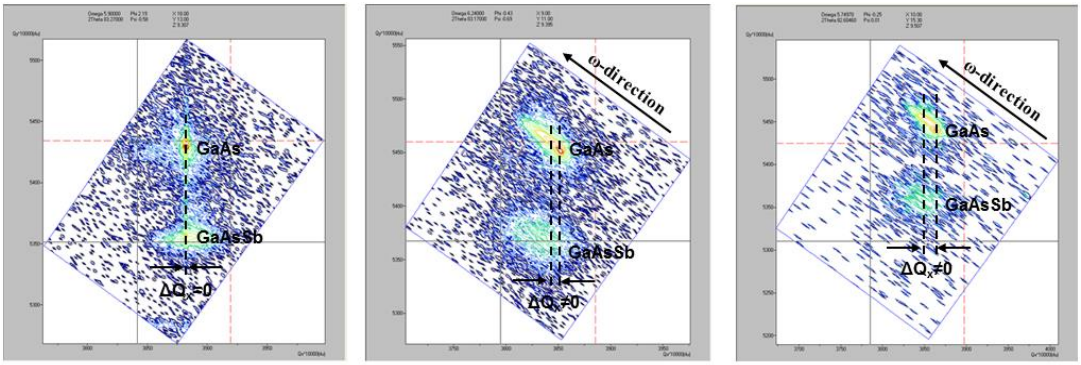

Fig. 4.4 XRD Reciprocal Space Maps in the Vicinity of the Asymmetrical (224) Reflections for the Samples A (Sb 7.3 %), B (Sb 9.8 %), and C (Sb 10.2 %)

the GaAs matrix. Such enhanced compressive strain increases the layer relaxation of GaAsSb. Furthermore, the diffraction spots around the GaAs substrate peak of the samples B and C are elongated along the ω-direction. This indicates that the topmost GaAs cap layer is partially tensile-stressed by the underlying GaAsSb layers with high Sb compositions [12].

Figure 4.5(a) shows the PL spectra of the QD samples at 4.2 K which are deconvoluted into the ground state (GS), E_0H_0, and two excite state (ES), E_1H_0 and E_1H_1, emissions. The GS peak energies are located at 1.132, 1.044, and 1.071 eV for the samples A, B, and C, respectively. The GS peak energy of the samples B and C is greatly redshifted by above ~60 meV relative to that of the sample A. This is due to the increased strain reducing effect on decreasing the in-plane compressive strain inside the QDs with increasing Sb composition [55]. In addition, the GS peak energy of the sample C is blueshifted by 27 meV with respect to that of the sample B, which is attributable to the change in QD shape from lens-shaped (sample B) to pyramidal-shaped QDs (sample C). Interestingly, the PL integrated intensity of the samples B and C with higher Sb compositions is significantly quenched by a factor of 20, as compared to the sample A (Sb 7.3 %). The increase of Sb composition deteriorates the crystal quality of the heterointerfaces between GaAs and GaAsSb, and generates misfit and threading dislocations in the QD stacks during the layer relaxation process. Such strain-induced crystalline defects trap photoexcited carriers and hence reduce the radiative recombination, leading to the poor PL efficiency [58].

To investigate the thermal behavior of carriers in the QDs, the PL peak energies of the GS emissions are plotted in Fig. 4.5(b). As the temperature increases the GS peak energies are shifted to the lower energy side (PL redshift) by interdot hopping process

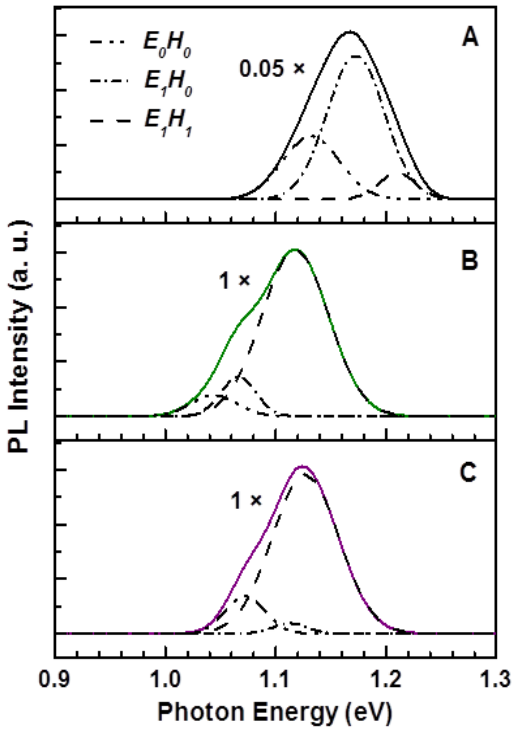

(a)

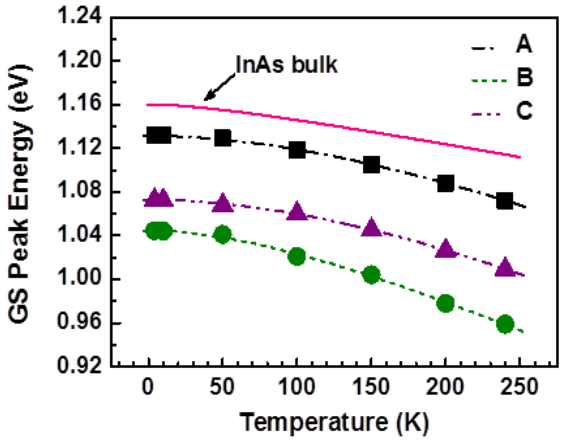

(b)

Fig. 4.5 (a) PL Spectra of the Samples A (Sb 7.3 %), B (Sb 9.8 %), and C (Sb 10.2 %) at 4.2 K (E_0, E_1: Ground and First Excited State in the Conduction Band/H_0, H_1: Ground and First Excited State in the Valence Band) and (b) GS Peak Energy Shift as a Function of Temperature

in the QDs [10]. The carriers are populated in the smaller QDs with high transition energy at low temperatures. However, as the temperature goes up, the carriers jump up to the larger QDs with low transition energy. The redshift rate with temperature of the sample A is faster than that of the InAs bulk and it becomes more faster with increasing Sb composition from 9.8 % to 10.2 %. The dependence of the redshift rate on Sb composition may be associated with the band structure change, which will be addressed in the following section.

Figure 4.6 displays the time-resolved PL (TRPL) decay transients of the GS emissions at 4.2 K for the QD structures. The integrated PL intensity of the QD emissions decreases exponentially with time. To determine the carrier lifetime in the QDs the TRPL spectra are fitted with the well-known biexponential decay function of [59]

$$I(t) = A_1 exp(-t/\tau_1) + A_2 exp(-t/\tau_2) \tag{4.1}$$

$$\tau_{avg} = \frac{\sum A_i \tau_i}{\sum A_i} \tag{4.2}$$

where I is the integrated PL intensity, $A_{1(2)}$ is the fitting constant, and $\tau_{1(2)}$ is the carrier lifetime. The average carrier lifetimes, τ_{avg}, of the samples A, B, and C are determined to be 1.7, 4.2, and 36.7 ns, respectively. The TRPL result reveals that the increase of Sb composition improves the carrier lifetime of the QDs. This can be explained by the transformation of the energy band structure. The increase of Sb composition causes the reduction of the VBO at the heterojunction between InAs and GaAsSb. Accordingly, holes are loosely confined in the valence band of QDs. This induces a weak Coulombic interaction between electrons and holes. As a result, carrier escape is enhanced and in turn the radiative recombination of carriers decreases, which is also estimated by the faster redshift rate of GS PL peak energy of the QDs with higher Sb composition.

In the view of the application of the QD-based IBSCs, the carrier lifetime is required to be improved in order to increase the carrier collection and thus photocurrent which is one of the most important device parameters to determine the conversion efficiency of IBSCs [49].

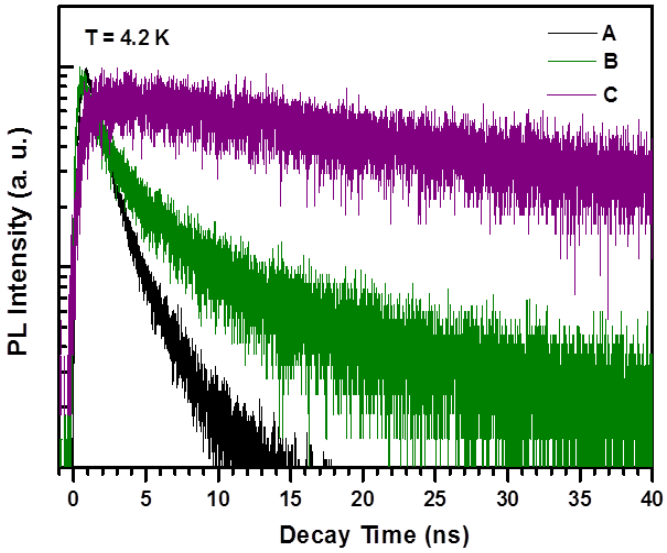

Fig. 4.6 TRPL Decay Curves Measured at the GS Emission Peaks of the QD Structures at 4.2 K

4.4 Conclusion

We have investigated the effect of Sb incorporation on the structural and optical properties of single- and multi-stack InAs/GaAsSb QDs. The increase of Sb composition in GaAsSb layers causes the change in QD morphologies such as QD density and height. In addition, it increases the strain relaxation of GaAsSb layers in the multi-stack QD structures due to the increased lattice mismatch strain at GaAs and GaAsSb interfaces. The strain reducing effect with increasing Sb composition causes a PL peak energy shift and increases carrier lifetime in the QDs because of the change in the band structure. From the experimental results, we have found that the increase of Sb composition is favorable to improving carrier lifetime of the QDs whereas it can degrade the crystal quality of the QD structure. Therefore, Sb composition should be well calibrated in order to employ InAs/GaAsSb QDs as a promising absorbing material for IBSCs.

Chapter 5

OPTIMIZATION OF SPACER LAYER THICKNESS OF MULTI-STACK INAS/GAASSB QUANTUM DOTS

5.1 Introduction

Semiconductor quantum dots (QDs) with zero-dimensional carrier confinement have been extensively studied for optoelectronic device applications as lasers, light-emitting diodes, and photodetectors due to their superior optical and electronic properties [60,61]. The strong carrier confinement of QDs has been applied to increase photocurrent of QD-based solar cells (QDSCs) by absorbing sub-bandgap photon energies [2,8]. The device performance of fabricated QDSCs has revealed that the photocurrent is slightly increased due to the small QD absorption volume, whereas the open-circuit voltage (V_{oc}) is highly reduced. As a result, the device performance of QDSCs is poorer compared with the reference solar cell without QDs.

To improve the device performance of QDSCs, InAs/GaAsSb QD systems have been recently introduced [9,62,63]. The increase in Sb composition of GaAsSb layers decreases the InAs QD size and increases the areal density of dots due to the Sb surfactant effect. Accordingly, the increased absorption volume of InAs QDs, embedded in GaAsSb layers with high Sb composition, allows absorbing more sub-bandgap photons [9]. Furthermore, the energy band alignment of InAs/GaAsSb heterojunctions changes from type-I to type-II alignment when Sb composition is above ~14 % [10]. In addition, the lattice mismatch between the InAs QDs and GaAsSb layers decreases with increasing Sb composition and thus the QDs are less strained. This leads to the reduction of V_{oc} loss of QDSCs because the generation of strain-induced crystalline defects is suppressed.

To use InAs/GaAsSb QDs as a potential absorbing material for QDSCs, the spacer layer thickness of GaAsSb is needed to be optimized because it affects strain distribution in the QD structure and hence electronic QD properties [64,65].

In this chapter, the structural and optical properties of ten-stack InAs/GaAsSb QDs with varying spacer layer thickness have been investigated. The strain relaxation of GaAsSb spacers increases with increasing the spacer thickness. The spacer thickness changes the crystalline defect density in the volume of GaAs and GaAsSb layers. Besides, it affects the interband optical transitions of carriers confined in the QDs.

5.2 Experimental Procedure

The multi-stack InAs/GaAsSb QD structures were grown by a solid-source molecular beam epitaxy system on n-type GaAs (001) substrates. A 400 nm-thick GaAs buffer layer was grown on the substrate, as shown in Fig. 5.1, at 600℃ after thermal deoxidation of the substrate surface. The substrate temperature was decreased to 500℃ to grow the QD stacks. Ten stacks of InAs QDs embedded in $GaAs_{0.83}Sb_{0.17}$ spacer layers were grown at the lowered substrate temperature. The QDs were grown in the Stranski–Krastanov growth mode by depositing 2 ML InAs on GaAsSb at a deposition rate of 0.04 ML/s. During InAs deposition, the reflection high-energy electron diffraction showed streaky to chevron patterns, which indicated the formation of self-assembled three-dimensional InAs QDs. To investigate the effect of spacer layer thickness, the GaAsSb spacer thicknesses (d_s) were varied to be 2, 5, 10, and 15 nm. A 50 nm-thick GaAs layer was finally grown on the InAs/GaAsSb QD stacks at an elevated substrate temperature of 600℃. The as-grown samples had type-II InAs/GaAsSb dots-in-a-well (DWELL) structure consisting of InAs QDs in GaAsSb quantum wells since the Sb composition (17 %) of the spacers is above ~14 %.

High-resolution x-ray diffraction (XRD) measurements were conducted using an X'Pert MRD diffractometer with $CuK_{\alpha 1}$ radiation (λ = 1.5406 Å) to estimate strain relaxation and crystalline defect density in the QD stacks. Transmission electron microscopy (TEM) measurements were carried out to observe the crystalline defects in the structures. Diffraction-contrast and high-resolution TEM images were recorded with an FEI-Philips CM200 operated at 200 keV and a JEOL JEM-4000 EX operated at 400 keV. For optical studies, continuous-wave photoluminescence (PL) measurements were done with a semiconductor laser (λ = 405 nm). The PL signals from

the samples loaded in a closed-cycle helium cryostat were detected using a liquid-nitrogen-cooled Ge photodiode and processed by a lock-in amplification technique.

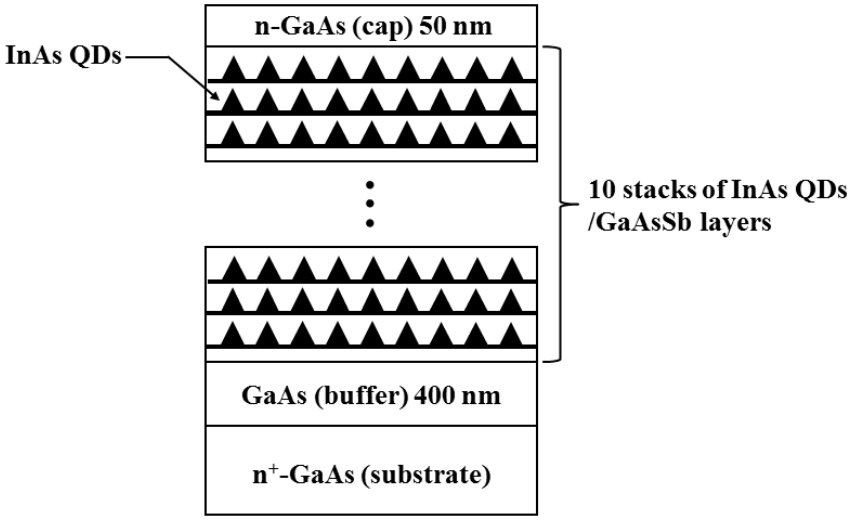

Fig. 5.1 Schematic Structure of Ten-stack Type-II InAs/GaAsSb QDs with Different Spacer Thicknesses of 2, 5, 10, and 15 nm

5.3 Results and Discussions

Figure 5.2 shows XRD reciprocal space maps (RSMs) in the vicinity of the asymmetrical (224) reflection to estimate the relaxation of initial elastic stress of the GaAsSb spacer layers. As d_s increases from 2 to 15 nm, the ΔQ_x in the RSMs increases indicating that the extent of strain relaxation of the GaAsSb increases with d_s. The strain relaxations of the GaAsSb are determined to be 0, 17, 40, and 67 % for the samples A, B, C, and D, respectively. The GaAsSb layers of the sample A (d_s = 2 nm) are pseudomorphically strained on the GaAs substrate. The increased lattice-mismatch stress at the GaAs/GaAsSb interfaces with thicker d_s results in the increasing strain relaxation from 17 to 67 %. In addition, diffraction spots around the GaAs and GaAsSb peaks are elongated along the ω-direction with increasing d_s. Such elongation of the diffraction spots can be caused by the partially relaxed GaAs cap layer, which is highly tensile-stressed by the underlying GaAsSb layers with increasing d_s [12].

Triple-crystal ω rocking curves (RCs) were measured in the vicinity of the symmetrical (004) reflections of the GaAs and GaAsSb peaks to derive the dislocation density in the volume of the structures. As shown in Fig. 5.3(a), the full-width-at-half-maximum (FWHM) of the ω RCs for GaAs increases with increasing d_s. From the FWHMs of the ω RCs, the dislocation density, ρ, is determined using the following equation [66].

$$\rho = \frac{\Delta D^2}{(2\pi \ln 2) \times b^2} \tag{5.1}$$

where ΔD is the FWHM of the ω RCs and b is the magnitude of the Burgers vectors. The values of ρ are calculated to be 1.7×10^5, 2.0×10^5, 3.9×10^5, and 9.4×10^6 cm^{-2} for the samples A, B, C, and D, respectively. It is noted that the dislocation density of the

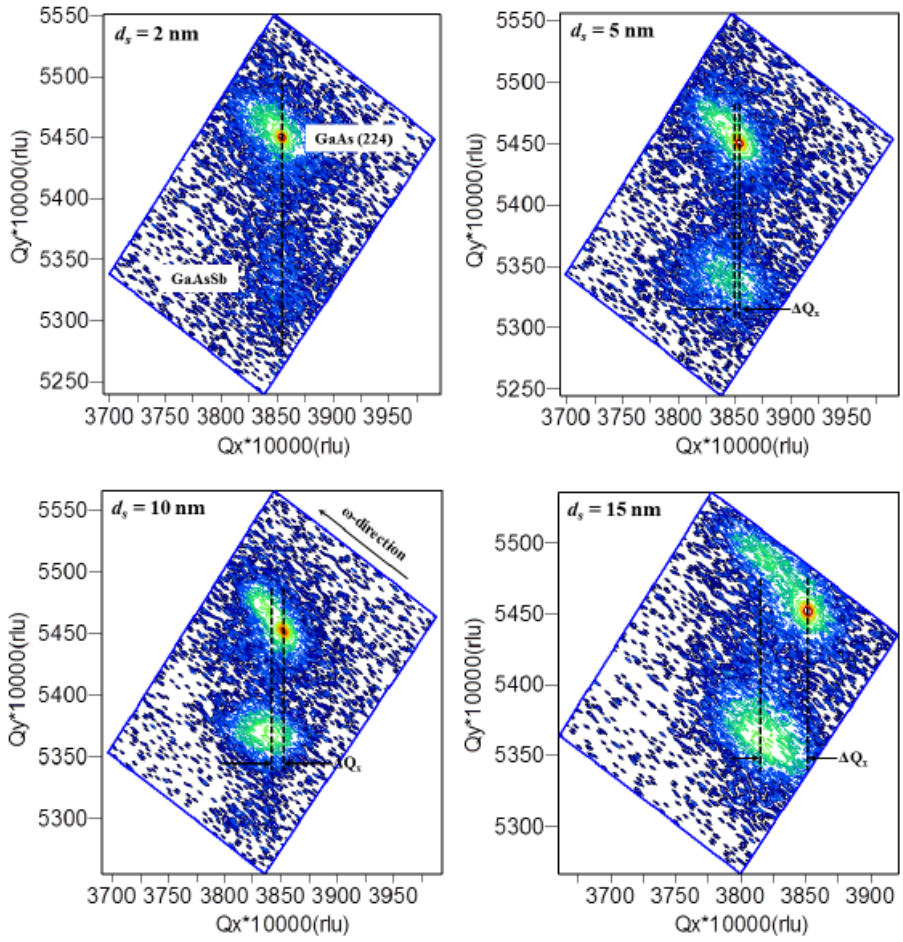

Fig. 5.2 XRD Reciprocal Space Maps from the Asymmetrical (224) Reflection of the QD Samples with Different d_s of 2, 5, 10, and 15 nm

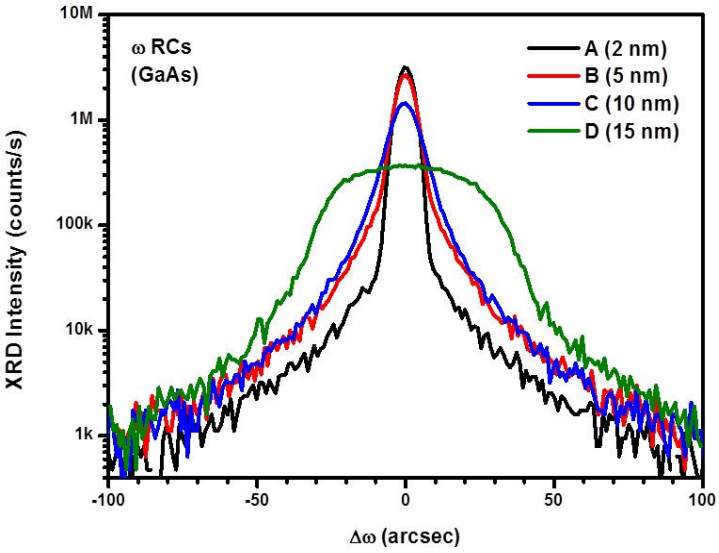

(a)

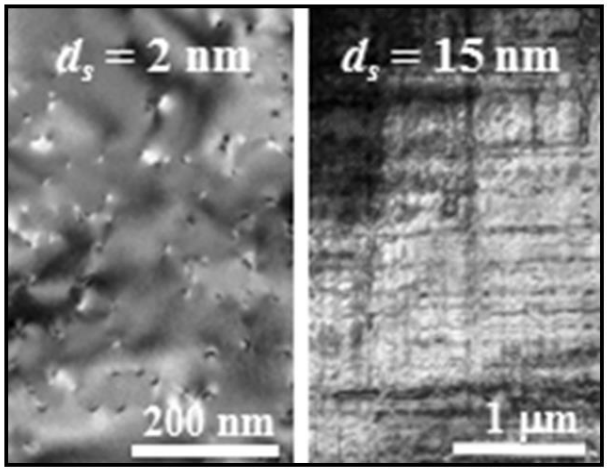

(b)

Fig. 5.3 (a) Triple-crystal XRD ω RCs in Vicinity of the Symmetrical (004) Reflection for the GaAs and (b) TEM Plan-view Images of the Samples A (d_s = 2 nm) and D (d_s = 15 nm)

sample D (d_s = 15 nm) is increased by more than an order of magnitude compared to those of the other samples. This is owing to the highly increased GaAsSb relaxation of 67 % because strain relaxation process generates significant crystalline defects such as misfit and threading dislocations in strained heterostructures [67,68]. Figure 5.3(b) displays plan-view TEM images of samples A (d_s = 2) and D (d_s = 15 nm). Compared to the sample A, cross-hatch dislocation patterns are observed in the TEM image of the sample D. These cross-hatch patterns are typically generated in highly deteriorated crystal structures [12,69].

In Fig. 5.4, the XRD intensity of ω RCs of the GaAsSb increases as d_s increases from 2 to 10 nm because of the increased number of diffracting GaAsSb planes. From the FWHMs of the ω RCs of the GaAsSb, the values of ρ are determined to be 1.7×10^9, 3.9×10^9, 1.5×10^9, and 3.6×10^9 cm^{-2} for the samples A, B, C, and D, respectively. The decreased coherence length arising from the high dislocation density in the GaAsSb layers causes the ω RC intensity of the sample D (d_s = 15 nm) to be reduced. Among the samples, the FWHM of the GaAsSb ω RC of the sample C (d_s = 10 nm) is the narrowest and hence it has the lowest dislocation density of 1.5×10^9 cm^{-2}. This can be ascribed to the reduced net strain of the GaAsSb layers resulting from the interplay between compressive strain by the GaAs and tensile strain by the InAs.

Figure 5.5 shows PL spectra of the samples A, B, C, and D with different d_s = 2, 5, 10, and 15 nm measured at 10 K. The PL peak energies of the ground state (GS) emissions are positioned at 1.076, 1.021, 1.105, and 1.015 eV while those of the excited state (ES) emissions are located at 1.086, 1.035, 1.136, and 1.071 eV for samples A, B, C, and D, respectively. The increase of d_s increases the in-plane lattice constant of the GaAsSb, which is confirmed by the increasing ΔQ_x of the RSMs. Therefore, the InAs QDs capped with GaAsSb layers are less compressive-strained with increasing d_s. It is

well known that a decreased compressive strain inside QDs gives rise to a PL redshift of QD emissions [70]. Meanwhile, a PL blueshift can be induced which results from the electronic decoupling of stacked QD layers by increasing d_s. In the vertically correlated QD structures, the electronic coupling between neighboring QD layers is stronger with decreasing d_s due to enhanced wavefunction overlap. Thus, miniband states in the conduction and valence bands of the QD structures are formed as QD layers are closely spaced. The miniband width increases as d_s decreases and hence electrons and holes are located at lower energy states of the minibands, leading to producing the PL redshift [71]. Another interesting point is that the energy separation (ΔE) between the GS and ES emission peaks is smaller with decreasing d_s. This is attributable to the strain-driven In/Ga intermixing at the heterointerfaces between InAs QDs and GaAsSb spacers in order to relieve the excess strain energy around the QDs. As d_s decreases the strain accumulation inside the QDs is larger, which is a driving force for the increased interdiffusion of In/Ga atoms. According to the report by Wang *et al.*, the energy separation between the GS and ES emissions of InAs QDs is reduced when In/Ga intermixing occurs [23]. This is in accordance with our observation of decreasing ΔE with decreasing d_s. Furthermore, it is found that the PL intensity ratio of ES to GS peaks is affected by d_s. The PL intensity ratio of ES to GS peaks increases with increasing d_s. The energy interval between the intersubband states becomes larger since the weak wavefunction overlap with increasing d_s suppresses the miniband formation and creates discrete energy levels in the QDs [71]. When discrete energy level spacing between intersubband states of QDs is large, carrier relaxation can be slow due to phonon bottleneck [72]. Consequently, it is plausible that carriers captured in the QDs recombine radiatively at higher energy states, which results in increasing the PL intensity ratio of ES to GS peaks with d_s.

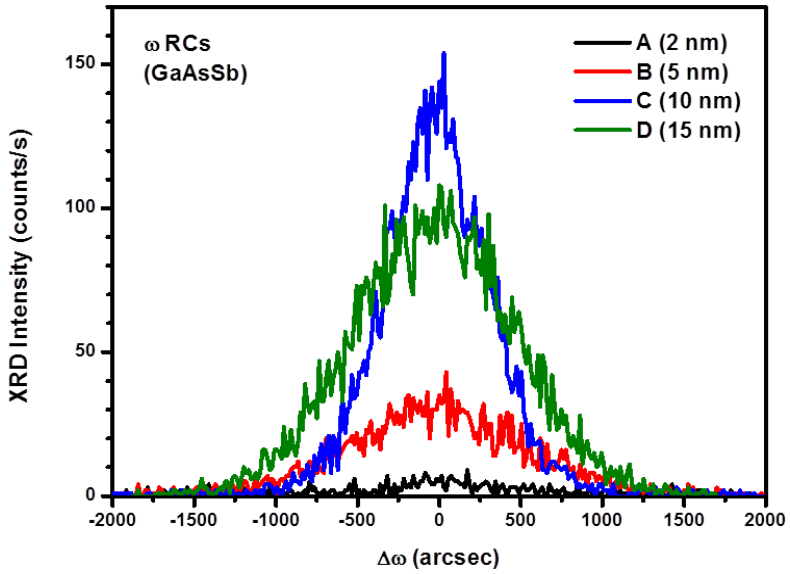

Fig. 5.4 Triple-crystal XRD ω RCs in Vicinity of the Symmetrical (004) Reflection for the GaAsSb

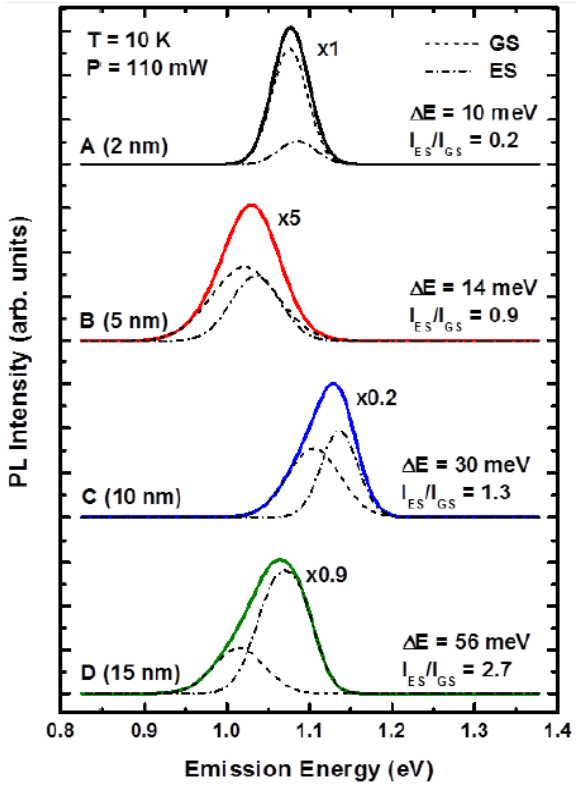

Fig. 5.5 PL Spectra of the Samples with Different Spacer Thicknesses at 10 K (The Values of ΔE and I_{ES}/I_{GS} Indicate the Energy Difference between the GS and ES Peak Energies and PL Intensity Ratio of ES to GS Peaks, Respectively)

Figure 5.6 exhibits the integrated PL intensities of the GS emissions according to excitation power at 10 K. The linearly increasing behavior of the PL intensities with excitation power on the log-log plot can be expressed as follows [73].

$$I = \eta P^k \tag{5.2}$$

where I is the integrated PL intensity, η is the luminescence efficiency, P is the excitation power density, and k is a coefficient. From the least-square fitting, the coefficients (k) are evaluated to be 0.94, 0.68, 0.98, and 1.39 for samples A, B, C, and D, respectively. The samples A and C show a linear dependence of the integrated PL intensity on excitation power ($k \approx 1$). On the other hand, the sample B exhibits a sublinear dependence of the integrated PL intensity on excitation power ($k < 1$). Such sublinear behavior of the PL intensity is attributed to the reduced PL efficiency caused by the increased nonradiative recombination in the QD stacks. As d_s is further increased to 15 nm, a superlinear behavior ($k > 1$) of the PL intensity with increasing excitation power is observed. It is reported that a superlinearity of PL intensity dependence can be caused by saturation of the nonradiative recombination centers at high excitation level in the InAs/InGaAs QD DWELL structures [74]. The number of photogenerated carriers increases with the d_s by optical excitation. Hence, the nonradiative recombination channels are strongly saturated by capturing the increased carriers, resulting in the superlinear PL intensity dependence of sample D (d_s = 15 nm).

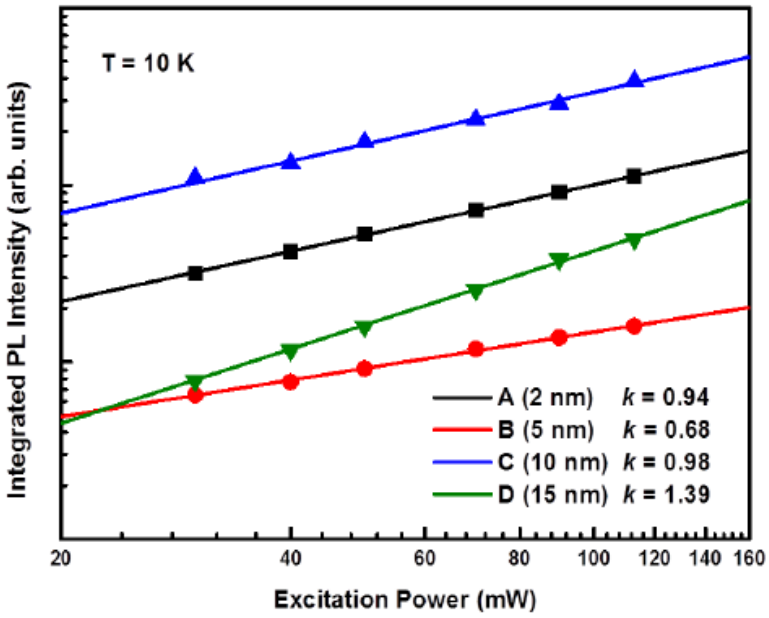

Fig. 5.6 Integrated PL Intensity of GS Emissions as a Function of Excitation Power at 10 K (The Solid Lines are the Least-square Fitted Lines using an $I \sim P^k$ Law)

5.4 Conclusion

To conclude, the effect of the spacer layer thickness on the structural and optical properties of ten-stack InAs/GaAsSb QDs has been investigated. The increase of d_s increases the extent of strain relaxation of the GaAsSb. The crystallinity of the GaAsSb is most enhanced when d_s = 10 nm, which may be due to reduced total strain. The PL peak energies of the QD emissions are affected by the counteracting effect of the PL redshift and blueshift with varying d_s. In particular, the QD structure (d_s = 10 nm) exhibits superior luminescence properties such as high PL efficiency and linear dependence of PL intensity on the excitation power. These experimental results suggest that the multi-stack InAs/GaAsSb QDs with an optimized spacer thickness can be used as a potential absorbing material for IBSCs.

Chapter 6

STRAIN-COMPENSATED INAS/GAASSB QUANTUM DOT SOLAR CELLS

6.1 Introduction

Self-assembled quantum dots (QDs) have been applied successfully to various optoelectronic devices because their discrete density of states and strong carrier confinement provide peculiar optical and electronic properties [4,75,76]. The quantum-confined states in QDs can be employed as a promising sub-bandgap photon absorber to increase photocurrent of QD-based solar cells (QDSCs) [4,62]. It is favorable to increase the number of the QD stacks for a high short-circuit current density (J_{sc}) owing to the extremely small absorption cross-section of QDs. However, the multi-stack QD structures are highly compressive strained with significant crystalline defects after growing 10–20 QD stacks, which decrease the J_{sc} of QDSCs [49]. In addition, the strong nonradiative recombination through strain-induced defects reduces low open-circuit voltage (V_{oc}) of QDSCs, leading to a significant drop in the conversion efficiency of QDSCs [77]. To reduce the strain accumulation in QD stacks, strain compensation layers (SCLs) such as GaP and GaNAs has been introduced [13,14]. The accumulated compressive strain in QD stacks is compensated by the tensile strain of the SCLs, leading to the reduction of the overall strain. Consequently, the strain-compensated QDSCs have shown improved J_{sc} and/or V_{oc} with high crystal quality.

The InAs/GaAsSb QDs with GaP SCLs, as an alternative to the InAs/GaAs QDs, are promising for QDSC applications since the surfactant effect of Sb results in increasing an areal QD density and thus improving sub-bandgap photon absorption [9]. Moreover, the InAs QDs are less strained by capping them with GaAsSb layers with a larger lattice constant than that of GaAs layers. This contributes to lowering the total strain of QD stacks [78]. In this chapter, we have studied the effects of the GaP SCLs

with different GaP coverages of 0, 1, 2, and 4 ML on the InAs/$GaAs_{0.95}Sb_{0.05}$ QDSCs. The high-resolution x-ray diffraction study reveals that the in-plane compressive strain of the QD structures is reduced from −1.24 to −0.39 % by the increased tensile strain of the GaP as increasing the GaP coverage from 0 to 4 ML. The photoluminescence spectra of the QD emissions are affected by the contrary effects of a PL redshift caused by the strain reduction inside the QDs and PL blueshift by the high potential barrier of the GaP. It is estimated from the external quantum efficiency spectra that the photocurrent by the QD absorption in the near infrared wavelengths is decreased with the GaP coverage from 1 to 4 ML while that by the GaAs matrix absorption in the wavelengths of 400–880 nm is increased. The increase of the GaP coverage from 0 to 2 ML improves the conversion efficiency from 7.22 to 9.44 % by the strain compensation effect. However, a further increase of the GaP coverage to 4 ML decreases the conversion efficiency by interfacial misfit dislocations around the GaP.

6.2 Experimental Procedure

The QDSCs with GaP layers were grown on p^+-type (001) GaAs substrates by using a solid-source molecular beam epitaxy system. As shown in Fig. 6.1, the solar cell structure consisted of a 50 nm n^+-type GaAs contact layer, a 50 nm n^+-type $Al_{0.8}Ga_{0.2}As$ window layer, a 150 nm n^+-type GaAs emitter layer, and a 1000 nm undoped GaAs base layer. Ten stacks of InAs (2 ML)/$GaAs_{0.95}Sb_{0.05}$ (10 nm) layers were grown at a substrate temperature of 500℃ in the middle of the base layer. The GaP layers with varying coverages of 1, 2, and 4 ML were embedded at the center of the GaAsSb layers as SCLs for the multi-stck QD structures. The chevron patterns were detected by reflection high-energy electron diffraction during the InAs deposition with a deposition rate of 0.04 ML/s. This is indicative of the formation of three-dimensional InAs QDs. Additional QDSC without GaP layers was grown under the same growth condition as a reference QD structure.

High-resolution x-ray diffraction (XRD) measurements were carried out using an X'Pert MRD diffractometer equipped with a $CuK_{\alpha 1}$ radiation (λ = 1.5406 Å) and hybrid four-bounce Ge (220) monochromator for structural characterization of the as-grown structures. For optical characterization photoluminescence (PL) measurements were peformed using a chopped semiconductor laser (λ = 532 nm) at 10 K. The PL signals were dispersed by a monochromator and detected by a cooled Ge detector interfaced with a lock-in amplifier.

The as-grown structures were fabricated to the solar cell devices using a conventional photolithography technique. The BCl_3-based reactive ion etching was used to electrically separate each solar cell device with a mesa size of (5×5 mm^2). The ohmic metals, Ge/Au/Ni/Au and Ti/Pt/Au, were deposited by an electron beam evaporator for the n-type and p-type contact of the devices, respectively. A double-layer

antireflection coating with SiO_2/SiN_x was applied to the front surface of the cells. Under one-sun illumination (100 mW/cm^2) at AM 1.5G condition, the external quantum efficiency (EQE) and current-voltage (*I-V*) characteristics of the fabricated cells were measured using a QEX10 system with a xenon arc lamp and Oriel Class A solar simulator, respectively.

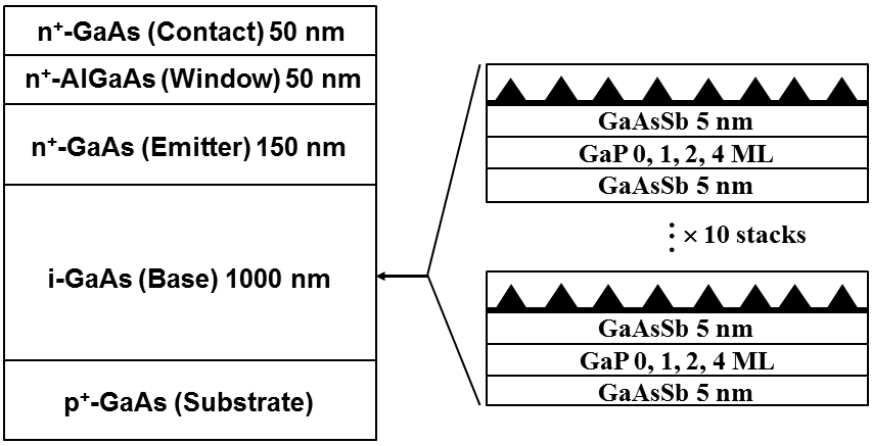

Fig. 6.1 Schematic Structure of Strain-compensated InAs/$GaAs_{0.95}Sb_{0.05}$ QDSCs with Different GaP Coverages of 0, 1, 2, and 4 ML

6.3 Results and Discussions

To study the effect of the introduction of the GaP layers on the elastic strain in the as-grown structures, double-crystal (DC) ω-2θ XRD rocking curves (RCs) in the vicinity of the (004) symmetrical reflection are measured as seen in Fig. 6.2(a). Each RC consists of the zeroth-order (0^{th}) satellite peak and higher order satellite peaks, which originate from the periodic InAs/GaAsSb superlattice structures. It is clearly observed that the 0^{th} satellite peak is gradually shifted to the GaAs substrate peak with increasing the GaP coverage. To determine the out-of-plane strain ($\varepsilon_{\perp}$) and in-plane strain ($\varepsilon_{\parallel}$) of the QD structures, the $\varepsilon_{\perp}$ is evaluated by the angular offset between the substrate peak and 0^{th} satellite peak in the ω-2θ RCs and the $\varepsilon_{\parallel}$ is estimated from the $\varepsilon_{\perp}$ using the following relations [79,80].

$$\varepsilon_{\parallel} = -\frac{(1-\nu)}{2\nu}\varepsilon_{\perp} = -\frac{(1-\nu)}{2\nu}\left[\frac{\sin\theta_B}{\sin(\theta_B+\Delta\theta)} - 1\right] \tag{6.1}$$

where ν is the Poisson's ratio, θ_B is the Bragg diffraction angle for the substrate, and $\Delta\theta$ is the angular difference between the substrate peak and 0^{th} satellite peak. As shown in Fig. 6.2(b), the increase of the GaP coverage results in the decrease of the tensile $\varepsilon_{\perp}$ from +1.06 to +0.33 % as well as the compressive $\varepsilon_{\parallel}$ from −1.24 to −0.39 %. It should be noted that the compressive $\varepsilon_{\parallel}$ in the QD structures is not fully compensated, even with using the GaP coverage of 4 ML. The GaP coverage for the strain balance ($\varepsilon_{\parallel} = 0$) in the structure is found to be ~5.8 ML by a linear regression analysis of the experimental data. The strain analysis presented here reveals that the tensile $\varepsilon_{\parallel}$ induced by the introduction of a few monolayers of GaP in the GaAs(Sb) matrix can effectively compensate the high compressive $\varepsilon_{\parallel}$ of the sample A without the GaP layers.

Figure 6.3 shows the PL spectra of the as-grown structures measured at 10 K with an excitation power density of 0.6 W/cm^2. Each PL spectrum is deconvoluted into

the two Gaussian bands of the ground state (GS) and first excited state (ES) emission denoted by E_0 and E_1, respectively. The PL peak positions of the GS and ES emission are located at 1.186/1.224, 1.203/1.265, 1.180/1.256, and 1.191/1.261 eV for the samples, A, B, C, and D, respectively. The non-monotonic shift of the PL peak energy according to the GaP coverage may be due to the counteracting effects of the introduction of the GaP. As confirmed in Fig. 6.2(b), the increase of the GaP coverage has an impact on reducing the compressive $\varepsilon_{\parallel}$ around the InAs QDs and thus the PL peak is redshifted [81,82]. Simultaneously, the effect of the confining potential barrier of the GaP is stronger with increasing the GaP coverage [83]. Such high potential barrier modifies the QD electronic levels, resulting in the blueshift of the QD emission [84,85]. Another remarkable feature of the PL spectra is that the energy separation (ΔE) between the GS and ES peak for the samples with the GaP layers is larger than that (ΔE = 38 meV) of the sample A. This is indicative of the enhanced QD confining potential effect by the insertion of the GaP layers [86,87]. As compared to the sample C the ΔE of the sample D (θ = 4 ML) is slightly decreased by 6 meV. It is expected that the average lateral QD dimension of the sample D is increased induced by the decrease of the compressive $\varepsilon_{\parallel}$ around the QDs. This increased lateral QD size can cause a slight decrease in the ΔE which is inversely coupled to the lateral confinement of the QDs [87].

Figure 6.4 shows the EQE spectra of the fabricated QDSCs at room temperature. As the GaP coverage increases from 0 to 4 ML the absorption-edge wavelength for the sub-band gap photons decreases from 1180 to 1050 nm. This trend is in accordance with the PL blueshift of the QD emissions at 294 K with the GaP coverages as seen in the inset of Fig. 6.4. To evaluate the J_{sc} from the photon absorption

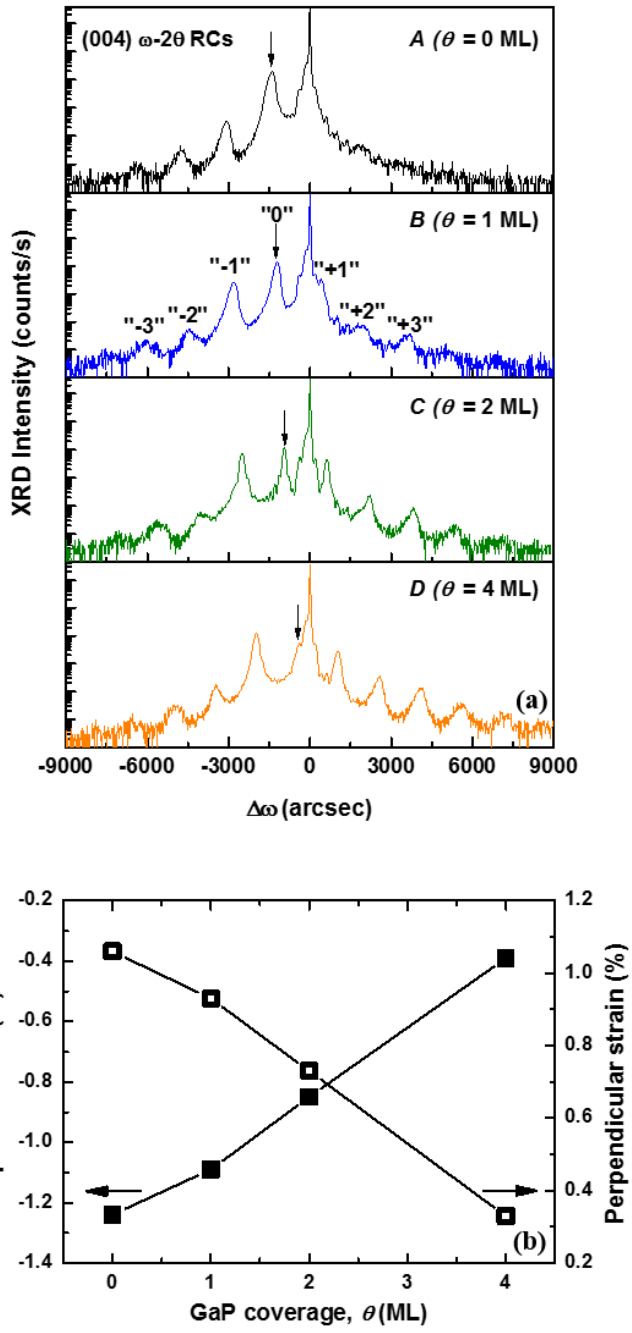

Fig. 6.2 (a) XRD ω-2θ RCs Scanned in the Vicinity of the GaAs(004) Reflection for the As-grown Structures with Different GaP Coverages of θ = 0, 1, 2, and 4 ML. (The 0^{th} Satellite Peaks are Indicated by an Arrow and Higher Order Satellite Peaks are Marked with ±1, ±2, ±3) (b) In-plane ($\varepsilon_{\parallel}$) and Out-of-plane Strain ($\varepsilon_{\perp}$) of the QD Structures as a Function of the GaP Coverage

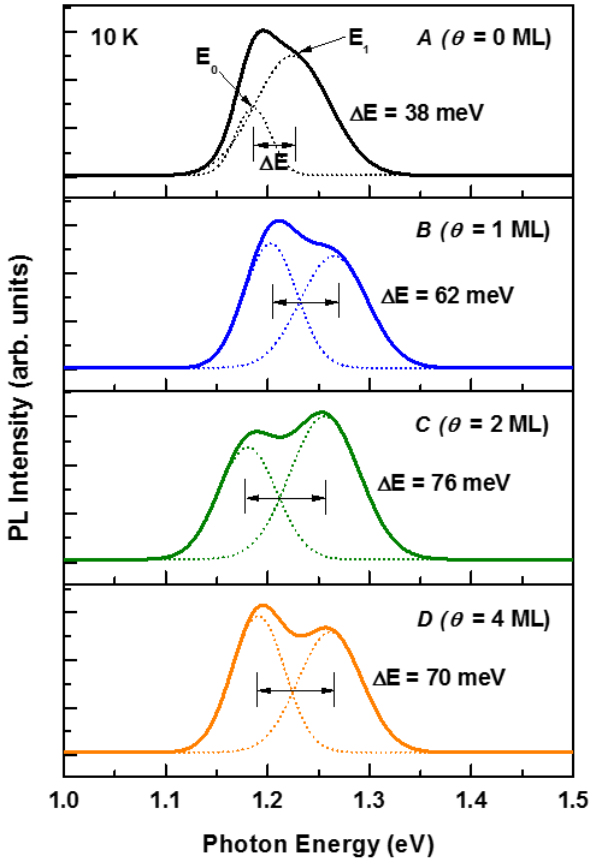

Fig. 6.3 PL Spectra of the Samples with Different GaP Coverages with an Excitation Power Density of 0.6 W/cm^2 at 10 K (E_0: Ground State Transition, E_1: First Excited State Transition, and ΔE: Energy Separation between the Observed Two Transitions)

by the QDs (880 nm < λ < 1050−1180 nm) and GaAs matrix (400 nm < λ < 880 nm) the EQE spectra are integrated with the incoming photon flux over the wavelength regions using the following equation [88].

$$J_{sc} = q\int \varphi_{ph}(\lambda) \cdot EQE(\lambda) d\lambda \tag{6.2}$$

where q is the electron charge, $\varphi_{ph}(\lambda)$ is the photon flux density under AM 1.5G spectrum, and EQE(λ) is the EQE in the wavelength regions. The $J_{SC(QD)}$, generated by the electron escape from the bound states of the QDs to continuum states in the conduction band, is decreased with increasing the GaP coverage as shown in Fig. 6.5. Itis found that the increase of a high potential barrier thickness increases the thermal emission time of the electrons confined at the sub-bands in QDs, leading to the reduction in the electron escape probability out of QDs [83]. Thus, the decreased $J_{SC(QD)}$ with the GaP coverage is ascribed to the suppressed electron escape by the enhanced confining effect. In addition, when the 1 ML of GaP is incorporated in the structure the $J_{SC(GaAs)}$ is reduced to 21.15 mA/cm^2 which may be due to the nonradiative recombination at the hetero-interfaces between the GaP and GaAs(Sb) matrix. On the other hand, the further increase of the GaP coverage from 1 to 4 ML increases the $J_{SC(GaAs)}$. This is because the increased in-plane tensile stress of the GaP with the coverages, as confirmed in Fig. 6.2(b), effectively offsets the compressive stress around the QDs, reducing the net strain of the QDSCs despite the increased lattice-mismatch between the GaP/GaAs(Sb) matrix. As a result, the overall crystal quality of the base and emitter layers is improved thanks to the less strain accumulation, leading to the increased $J_{SC(GaAs)}$.

Figure 6.6 shows the *I-V* characteristics of the QDSCs illuminated at one-sun intensity (100 mW/cm^2) with AM 1.5G spectrum and the device performance parameters are listed in Table 6.1. The V_{oc} of the QDSCs with the GaP layers is higher

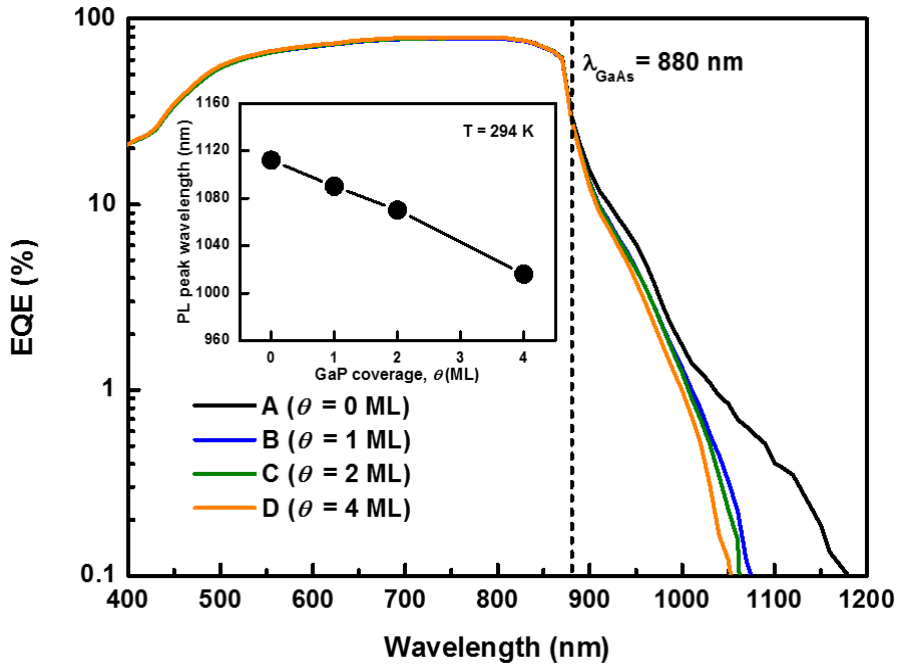

Fig. 6.4 EQE Spectra of the Fabricated QDSCs with Varying GaP Coverages (The Inset Illustrates the PL Peak Shift according to the GaP Coverage at 294 K)

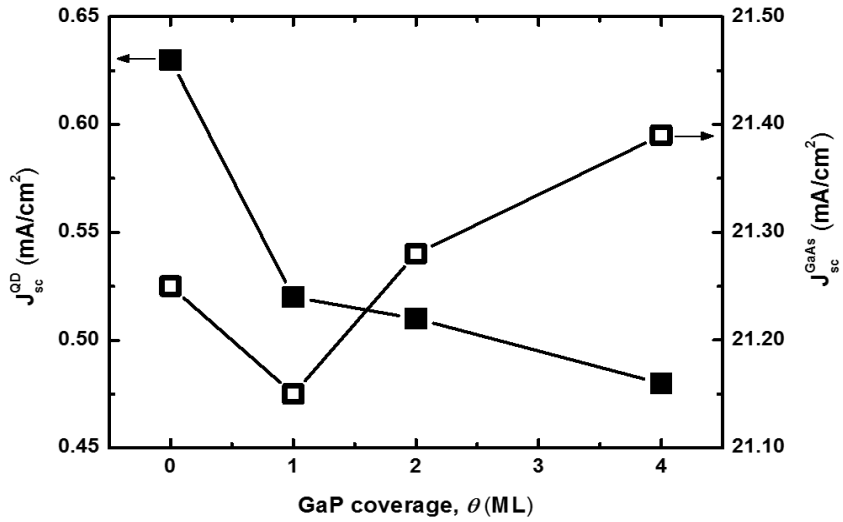

Fig. 6.5 $J_{SC(QD)}$ and $J_{SC(GaAs)}$ as a Function of the GaP Coverage Calculated from the EQE Spectra with Eq. (6.2)

by above 20 mV with respect to that (0.585 V) of the sample A as a result of the V_{oc} recovery by the strain compensation effect of the GaP [13,32]. Interestingly, the V_{oc} is reduced with increasing the GaP coverage from 1 to 4 ML. The reduced V_{oc} with the GaP coverage may be due to the increased nonradiative recombination through interface misfit dislocations in the depletion region of the QDSCs which limits the minority carrier transport [89,90]. To correlate the onset of the misfit dislocation generation with the decreased V_{oc} with the GaP coverage, the critical thickness (h_c) of the GaP for misfit dislocation nucleation is calculated based on the Matthews-Blakeslee model [91].

$$h_c = \frac{\mathrm{b}}{2\pi f}\frac{(1-\upsilon\cos^2\alpha)}{(1+\upsilon)\cos\lambda}\left(\ln\frac{h_c}{\mathrm{b}}+1\right) \tag{6.3}$$

where the b is the magnitude of the Burgers vector (**b**) of the misfit dislocation, f is the lattice mismatch between the substrate and GaP (f = 0.036), ν is the Poisson's ratio of the substrate (ν = 0.31), α is the angle between the misfit dislocation line (**u**) and its **b**, and λ is the angle between the **b** and the vector which is perpendicular to both the **u** and the surface normal vector. It is assumed that the misfit dislocations are 60° a/2 <110> {111} dislocations (b = a / $\sqrt{2}$) and their **b** is inclined at 45˚ to (001) planes (cosα = cosλ = 1/2) [92,93]. The corresponding h_c of the GaP is determined to be 10.7 nm, which is comparable to the total GaP coverage of 40 ML (10.8 nm) in the QDSC D. Therefore, the total thickness (h) of the GaP layers is closer to the h_c of the GaP with increasing the GaP coverage from 1 to 4 ML. When the h exceeds the h_c the onset of the elastic strain relaxation is expected to release the elastic strain energy, accompanied by the misfit dislocation formation [94,95]. Such misfit dislocations are responsible for the reduced V_{oc} of the QDSC D since they decrease the minority carrier lifetime and diffusion length. Additionally, the misfit dislocations tend to accompany threading

dislocations propagating from the interface into the growth front, which can act as a shunt current path leading to the reduction in the fill factor (FF) of the QDSC D [68,95]. Even though the introduction of the GaP helps to improve the V_{oc} of the QDSCs by reducing the $\varepsilon_{\parallel}$, the increase of the GaP coverage to 4 ML degrades the V_{oc} and FF of the QDSC D because of the limited h_c. As a result, the conversion efficiency (η) of the QDSCs is increased from 7.22 to 9.44 % with increasing the GaP coverage from 0 to 2 ML and then it is decreased to 8.20 %with a further increase in the GaP coverage to 4 ML. From the *I-V* analysis it is stressed that the GaP coverage should be well optimized to maximize the strain compensation effect under the condition of $h < h_c$ for the high-performance QDSCs.

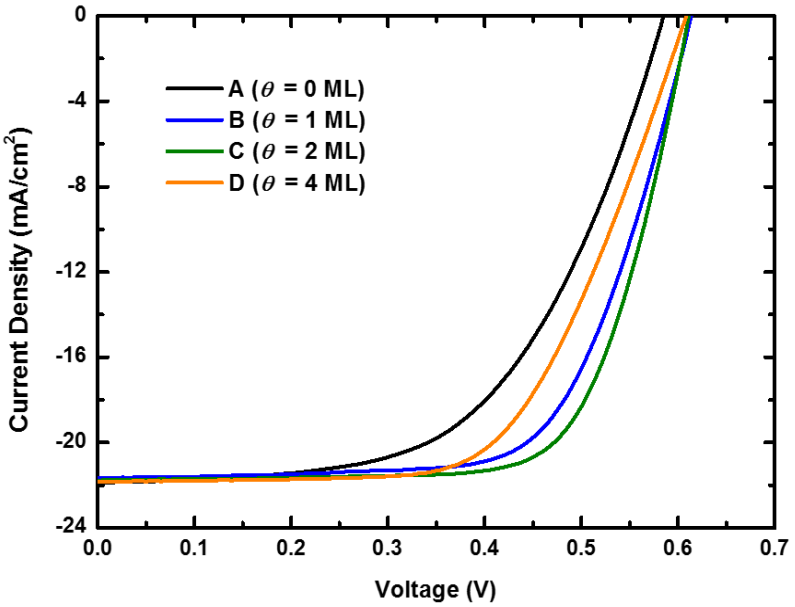

Fig. 6.6 *I-V* Characteristics of the Fabricated QDSCs with Varying GaP Coverage under One-sun Illumination (100 mW/cm^2) at AM 1.5G

Sample	V_{oc} (V)	J_{sc} (mA/cm^2)	FF (%)	η (%)
A (θ = 0 ML)	0.585	21.88	56.4	7.22
B (θ = 1 ML)	0.613	21.67	67.0	8.90
C (θ = 2 ML)	0.612	21.79	70.8	9.44
D (θ = 4 ML)	0.608	21.87	61.7	8.20

Table 6.1 Device Performance Parameters Derived from the Illuminated *I-V* Characteristics of the Fabricated QDSCs

6.4 Conclusion

In conclusion, we have studied the strain compensation effect of the GaP on the InAs/GaAsSb QDSCs with different GaP coverages. The increase of the GaP coverage reduces the compressive $\varepsilon_{\parallel}$ of the QD stacks by the enhanced strain compensation effect. The observed PL behavior with the GaP coverage is a result of the competing PL redshift and blueshift by the reduced strain in the QDs and increased confining potential of the GaP, respectively. The EQE spectral response in the near IR regions by the QD absorption is weakened, leading to the reduced IR photocurrent with the GaP coverage from 1 to 4 ML. On the contrary, the reduced strain accumulation with the increased GaP coverages improves the crystal quality of the structures, resulting in the enhanced EQE response in the absorption wavelengths of the GaAs matrix. The *I-V* data exhibit that the strain compensation by the GaP increases the conversion efficiency of the QDSCs with $h < h_c$. The experimental results suggest that the device performance of the QDSCs can be further improved by optimizing the GaP coverage under the critical thickness criteria for the GaP.

REFERENCES

[1] W. Shockley and H. J. Queisser, "Detailed balance limit of efficiency of p-n junction solar cells," *J. Appl. Phys.*, vol. 32, pp. 510–519, 1961.

[2] A. Luque and A. Martí, "Increasing the Efficiency of Ideal Solar Cells by Photon Induced Transitions at Intermediate Levels," *Phys. Rev. Lett.*, vol. 78, pp. 5014–5017, 1997.

[3] R. D. Schaller and V. I. Klimov, "High efficiency carrier multiplication in PbSe nanocrystals: Implications for solar energy conversion," *Phys. Rev. Lett.*, vol. 92, p. 186601, 2004.

[4] A. Martí, E. Antolín, C. R. Stanley, C. D. Farmer, N. López, P. Díaz, E. Cánovas, P. G. Linares, and A. Luque, "Production of photocurrent due to intermediate-to-conduction-band transitions: A demonstration of a key operating principle of the intermediate-band solar cell," *Phys. Rev. Lett.*, vol. 97, p. 247701, 2006.

[5] A. Luque, A. Martí, C. Stanley, N. López, L. Cuadra, D. Zhou, J. L. Pearson, and A. McKee, "General equivalent circuit for intermediate band devices: Potentials, currents and electroluminescence," *J. Appl. Phys.*, vol. 96, p. 903, 2004.

[6] D. F. Marrón, E. Cánovas, I. Artacho, C. R. Stanley, M. Steer, T. Kaizu, Y. Shoji, N. Ahsan, Y. Okada, E. Barrigón, I. Rey-Stolle, C. Algora, A. Martí, and A. Luque, "Application of photoreflectance to advanced multilayer structures for photovoltaics," *Mater. Sci. Eng. B*, vol. 178, pp. 599–608, 2013.

[7] D. Zhou, G. Sharma, S. F. Thomassen, T. W. Reenaas, and B. O. Fimland, "Optimization towards high density quantum dots for intermediate band solar cells grown by molecular beam epitaxy," *Appl. Phys. Lett.*, vol. 96, p. 061913, 2010.

[8] A. Luque and A. Martí, "The intermediate band solar cell: Progress toward the realization of an attractive concept," *Adv. Mater.*, vol. 22, pp. 160–174, 2010.

[9] K.-Y. Ban, S. P. Bremner, G. Liu, S. N. Dahal, P. C. Dippo, A. G. Norman, and C. B. Honsberg, "Use of a GaAsSb buffer layer for the formation of small, uniform, and dense InAs quantum dots," *Appl. Phys. Lett.*, vol. 96, p. 183101, 2010.

[10] K.-Y. Ban, D. Kuciauskas, S. P. Bremner, and C. B. Honsberg, "Observation of band alignment transition in InAs/GaAsSb quantum dots by photoluminescence," *J. Appl. Phys.*, vol. 111, p. 104302, 2012.

[11] J. T. Ng, U. Bangert, and M. Missous, "Formation and role of defects in stacked large binary InAs/GaAs quantum dot structures," *Semicond. Sci. Technol.*, vol. 22, pp. 80–85, 2007.

[12] S. P. Bremner, K.-Y. Ban, N. N. Faleev, C. B. Honsberg, and D. J. Smith, "Impact of stress relaxation in GaAsSb cladding layers on quantum dot creation in InAs/GaAsSb structures grown on GaAs (001)," *J. Appl. Phys.*, vol. 114, p. 103511, 2013.

[13] R. B. Laghumavarapu, M. El-Emawy, N. Nuntawong, A. Moscho, L. F. Lester, and D. L. Huffaker, "Improved device performance of InAsGaAs quantum dot solar cells with GaP strain compensation layers," *Appl. Phys. Lett.*, vol. 91, p. 243115, 2007.

[14] R. Oshima, T. Hashimoto, H. Shigekawa, and Y. Okada, "Multiple stacking of self-assembled InAs quantum dots embedded by GaNAs strain compensating layers," *J. Appl. Phys.*, vol. 100, p. 083110, 2006.

[15] E. Antolín, A. Martí, C. D. Farmer, P. G. Linares, E. Hernández, A. M. Sánchez, T. Ben, S. I. Molina, C. R. Stanley, and A. Luque, "Reducing carrier escape in the InAs/GaAs quantum dot intermediate band solar cell," *J. Appl. Phys.*, vol. 108, p. 064513, 2010.

[16] H. Lüth, *Solid Surfaces, Interfaces and Thin Films*, Springer, 2010.

[17] J. M. Moison, F. Houzay, F. Barthe, L. Leprince, E. André, and O. Vatel, "Self-organized growth of regular nanometer-scale InAs dots on GaAs," *Appl. Phys. Lett.*, vol. 64, p. 196, 1994.

[18] J. M. Ulloa, I. W. D. Drouzas, P. M. Koenraad, D. J. Mowbray, M. J. Steer, H. Y. Liu, and M. Hopkinson, "Suppression of InAs/GaAs quantum dot decomposition by the incorporation of a GaAsSb capping layer," *Appl. Phys. Lett.*, vol. 90, p. 213105, 2007.

[19] S. J. Lee, N. H. Shin, J. J. Ko, M. J. Park, and R. Kummel, "Density of states of quantum dots and crossover from 3D to Q0D electron gas," *Semicond. Sci. Technol.*, vol. 7, pp. 1072–1079, 1992.

[20] J. R. Chelikowsky and M. L. Cohen, "Nonlocal pseudopotential calculations for the electronic structure of eleven diamond and zinc-blende semiconductors," *Phys. Rev. B*, vol. 14, p. 556, 1976.

[21] S. N. Dahal, S. P. Bremner, and C. B. Honsberg, "Band structure calculation for quantum dot solar cells using k.p method," *33rd IEEE Photovolt. Spec. Conf.*, E-ISBN: 978-1-4244-1641-7, 2008.

[22] T. M. Hsu, Y. S. Lan, W.-H. Chang, N. T. Yeh, and J.-I. Chyi, "Tuning the energy levels of self-assembled InAs quantum dots by rapid thermal annealing," *Appl. Phys. Lett.*, vol. 76, p. 691, 2000.

[23] X. C. Wang, S. J. Xu, S. J. Chua, Z. H. Zhang, W. J. Fan, C. H. Wang, J. Jiang, and X. G. Xie, "Widely tunable intersubband energy spacing of self-assembled InAs/GaAs quantum dots due to interface intermixing," *J. Appl. Phys.*, vol. 86, p. 2687, 1999.

[24] L.-W. Wang, J. Kim, and A. Zunger, "Electronic structures of [110]-faceted self-assembled pyramidal InAs/GaAs quantum dots," *Phys. Rev. B*, vol. 59, p. 5678, 1999.

[25] M. Ohring, *The Material Science of Thin Films*, Academic Press, 1992.

[26] V. LaBella, H. Yang, D. Bullock, P. Thibado, P. Kratzer, and M. Scheffler, "Atomic Structure of the GaAs(001)-(2×4) Surface Resolved Using Scanning Tunneling Microscopy and First-Principles Theory," *Phys. Rev. Lett.*, vol. 83, pp. 2989, 1999.

[27] V. P. LaBella, M. R. Krause, Z. Ding, and P. M. Thibado, "Arsenic-rich GaAs(001) surface structure," *Surf. Sci. Rep.*, vol. 60, pp. 1–53, 2005.

[28] K. Seshan, *Handbook of Thin Film Deposition*, Elsevier, 2012.

[29] W. Shockley and W. T. Read, "Statistics of the Recombinations of Holes and Electrons," *Phys. Rev.*, vol. 87, p. 835, 1952.

[30] M. A. Green, *Operating Principles, Technology and System Applications*, Prentice-Hall, 1982.

[31] S. A. Blokhin, A. V. Sakharov, A. M. Nadtochy, A. S. Pauysov, M. V. Maximov, N. N. Ledentsov, A. R. Kovsh, S. S. Mikhrin, V. M. Lantratov, S. A. Mintairov, N. A. Kaluzhniy, and M. Z. Shvarts, "AlGaAs/GaAs photovoltaic cells with an array of InGaAs QDs," *Semiconductors*, vol. 43, pp. 514–518, 2009.

[32] S. M. Hubbard, C. D. Cress, C. G. Bailey, R. P. Raffaelle, S. G. Bailey, and D. M. Wilt, "Effect of strain compensation on quantum dot enhanced GaAs solar cells," *Appl. Phys. Lett.*, vol. 92, p. 123512, 2008.

[33] R. Oshima, A. Takata, Y. Shoji, K. Akahane, and Y. Okada, "InAs/GaNAs strain-compensated quantum dots stacked up to 50 layers for use in high-efficiency solar cell," *Phys. E*, vol. 42, pp. 2757–2760, 2010.

[34] I. P. Marko, N. F. Massé, S. J. Sweeney, A. D. Andreev, A. R. Adams, N. Hatori, and M. Sugawara, "Carrier transport and recombination in p-doped and intrinsic 1.3μm InAs/GaAs quantum-dot lasers," *Appl. Phys. Lett.*, vol. 87, p. 211114, 2005.

[35] S.-F. Tang, S.-Y. Lin, and S.-C. Lee, "Near-room-temperature operation of an InAs/GaAs quantum-dot infrared photodetector," *Appl. Phys. Lett.*, vol. 78, p. 2428, 2001.

[36] H. Y. Liu, M. J. Steer, T. J. Badcock, D. J. Mowbray, M. S. Skolnick, P. Navaretti, K. M. Groom, M. Hopkinson, and R. A. Hogg, "Long-wavelength light emission and lasing from InAs/GaAs quantum dots covered by a GaAsSb strain-reducing layer," *Appl. Phys. Lett.*, vol. 86, p. 143108, 2005.

[37] K.-Y. Ban, W.-K. Hong, S. P. Bremner, S. N. Dahal, H. Mcfelea, and C. B. Honsberg, "Controllability of the subband occupation of InAs quantum dots on a delta-doped GaAsSb barrier," *J. Appl. Phys.*, vol. 109, p. 014312, 2011.

[38] T. T. Chen, C. L. Cheng, Y. F. Chen, F. Y. Chang, H. H. Lin, C.-T. Wu, and C.-H. Chen, "Unusual optical properties of type-II InAs⁄$GaAs_{0.7}Sb_{0.3}$ quantum dots by photoluminescence studies," *Phys. Rev. B*, vol. 75, p. 033310, 2007.

[39] Y. D. Jang, T. J. Badcock, D. J. Mowbray, M. S. Skolnick, J. Park, D. Lee, H. Y. Liu, M. J. Steer, and M. Hopkinson, "Carrier lifetimes in type-II InAs quantum dots capped with a GaAsSb strain reducing layer Carrier lifetimes in type-II InAs quantum dots capped with a GaAsSb strain reducing layer," *Appl. Phys. Lett.*, vol. 92, p. 251905, 2008.

[40] Y. S. Chiu, M. H. Ya, W. S. Su, and Y. F. Chen, "Properties of photoluminescence in type-II GaAsSb/GaAs multiple quantum wells," *J. Appl. Phys.*, vol. 92, p. 5810, 2002.

[41] K. Gundogdu, K. C. Hall, T. F. Boggess, D. G. Deppe, and O. B. Shchekin, "Ultrafast electron capture into p-modulation-doped quantum dots," *Appl. Phys. Lett.*, vol. 85, p. 4570, 2004.

[42] J. Phillips, K. Kamath, X. Zhou, N. Chervela, and P. Bhattacharya, "Photoluminescence and far-infrared absorption in Si-doped self-organized InAs quantum dots," *Appl. Phys. Lett.*, vol. 71, p. 2079, 1997.

[43] Y. P. Varshni, "Temperature dependence of the energy gap in semiconductors," *Physica*, vol. 34, pp. 149–154, 1967.

[44] E. F. Schubert, "Delta doping of III–V compound semiconductors: Fundamentals and device applications," *J. Vac. Sci. Technol. A*, vol. 8, p. 2980, 1990.

[45] P. W. Fry, I. E. Itskevich, D. J. Mowbray, M. S. Skolnick, J. J. Finley, J. A. Barker, E. P. O. Reilly, L. R. Wilson, I. A. Larkin, P. A. Maksym, M. Hopkinson, J. P. R. David, A. G. Cullis, G. Hill, and J. C. Clark, "Inverted Electron-Hole Alignment in InAs-GaAs Self-Assembled Quantum Dots," *Phys. Rev. Lett.*, vol. 84, p. 733, 2000.

[46] R. Duan, B. Wang, Z. Zhu, and Y. Zeng, "Silicon Doping Induced Increment of Quantum Dot Density," *Jpn. J. Appl. Phys.*, vol. 42, pp. 6314–6318, 2003.

[47] Y.-A. Liao, W.-T. Hsu, M.-C. Lee, P.-C. Chiu, J.-I. Chyi, and W.-H. Chang, "Time-resolved photoluminescence of type-II InAs/GaAs quantum dots covered by a thin $GaAs_{1-x}Sb_x$ layer," *Phys. Status Solidi C*, vol. 6, pp. 1449–1452, 2009.

[48] J. Siegert, S. Marcinkevičius, and Q. X. Zhao, "Carrier dynamics in modulation-doped InAs⁄GaAs quantum dots," *Phys. Rev. B*, vol. 72, p. 085316, 2005.

[49] A. Martí, N. López, E. Antolín, E. Cánovas, A. Luque, C. R. Stanley, C. D. Farmer, and P. Díaz, "Emitter degradation in quantum dot intermediate band solar cells," *Appl. Phys. Lett.*, vol. 90, p. 233510, 2007.

[50] A. J. Nozik, M. C. Beard, J. M. Luther, M. Law, R. J. Ellingson, and J. C. Johnson, "Semiconductor quantum dots and quantum dot arrays and applications of multiple exciton generation to third-generation photovoltaic solar cells," *Chem. Rev.*, vol. 110, p. 6873, 2010.

[51] V. M. Ustinov, N. A. Maleev, A. E. Zhukov, A. R. Kovsh, A. Yu. Egorov, A. V. Lunev, B. V. Volovik, I. L. Krestnikov, Yu. G. Musikhin, N. A. Bert, P. S. Kop'ev, Zh. I. Alferov, N. N. Ledentsov, and D. Bimberg, "InAs/InGaAs quantum dot structures on GaAs substrates emitting at 1.3 μm," *Appl. Phys. Lett.*, vol. 74, p. 2815, 1999.

[52] G. Medeiros Ribeiro, D. Leonard, and P. M. Petroff, "Electron and hole energy levels in InAs self-assembled quantum dots," *Appl. Phys. Lett.*, vol. 66, p. 1767, 1995.

[53] Z. R. Wasilewski, S. Fafard, and J. P. McCaffrey, "Size and shape engineering of vertically stacked self-assembled quantum dots," *J. Cryst. Growth*, vol. 201-202, pp. 1131–1135, 1999.

[54] M. Grundmann, O. Stier, and D. Bimberg, "InAs/GaAs pyramidal quantum dots: Strain distribution, optical phonons, and electronic structure," *Phys. Rev. B*, vol. 52, p. 11969, 1995.

[55] K. Akahane, N. Yamamoto, S.-i. Gozu, and N. Ohtani, "Strong photoluminescence and laser operation of InAs quantum dots covered by a GaAsSb strain-reducing layer," *Physica E*, vol. 26, pp. 395–399, 2005.

[56] M. Bozkurt, J. M. Ulloa, and P. M. Koenraad, "An atomic scale study on the effect of Sb during capping of MBE grown III–V semiconductor QDs," *Semicond. Sci. Technol.*, vol. 26, p. 064007, 2011.

[57] Q. Xie, A. Madhukar, P. Chen, and N. P. Kobayashi, "Vertically Self-Organized InAs Quantum Box Islands on GaAs(100)," *Phys. Rev. Lett.*, vol. 75, p. 2542, 1995.

[58] T. Inoue, S. Kido, K. Sasayama, T. Kita, and O. Wada, "Impurity doping in self-assembled InAs/GaAs quantum dots by selection of growth steps," *J. Appl. Phys.*, vol. 108, p. 063524, 2010.

[59] W. Fang, J. Y. Xu, a Yamilov, H. Cao, Y. Ma, S. T. Ho, and G. S. Solomon, "Large enhancement of spontaneous emission rates of InAs quantum dots in GaAs microdisks," *Opt. Lett.*, vol. 27, pp. 948–950, 2002.

[60] J. X. Chen, A. Markus, A. Fiore, U. Oesterle, R. P. Stanley, J. F. Carlin, R. Houdré, M. Ilegems, L. Lazzarini, L. Nasi, M. T. Todaro, E. Piscopiello, R. Cingolani, M. Catalano, J. Katcki, and J. Ratajczak, "Tuning InAs/GaAs quantum dot properties under Stranski-Krastanov growth mode for 1.3 μm applications," *J. Appl. Phys.*, vol. 91, p. 6710, 2002.

[61] S.-W. Lee, K. Hirakawa, and Y. Shimada, "Bound-to-continuum intersubband photoconductivity of self-assembled InAs quantum dots in modulation-doped heterostructures," *Appl. Phys. Lett.*, vol. 75, p. 1428, 1999.

[62] W.-S. Liu, H.-M. Wu, F.-H. Tsao, T.-L. Hsu, and J.-I. Chyi, "Improving the characteristics of intermediate-band solar cell devices using a vertically aligned InAs/GaAsSb quantum dot structure," *Sol. Energy Mater. Sol. Cells*, vol. 105, pp. 237–241, 2012.

[63] W.-S. Liu, H.-M. Wu, Y.-A. Liao, J.-I. Chyi, W.-Y. Chen, and T.-M. Hsu, "High optical property vertically aligned InAs quantum dot structures with GaAsSb overgrown layers," *J. Cryst. Growth*, vol. 323, pp. 164–166, 2011.

[64] A. Alguno, N. Usami, T. Ujihara, K. Fujiwara, G. Sazaki, K. Nakajima, K. Sawano, and Y. Shiraki, "Effects of spacer thickness on quantum efficiency of the solar cells with embedded Ge islands in the intrinsic layer," *Appl. Phys. Lett.*, vol. 84, p. 2802, 2004.

[65] H. Heidemeyer, S. Kiravittaya, C. Muller, N. Y. Jin Phillipp, and O. G. Schmidt, "Closely stacked InAs/GaAs quantum dots grown at low growth rate," *Appl. Phys. Lett.*, vol. 80, p. 1544, 2002.

[66] J. E. Ayers, "The measurement of threading dislocation densities in semiconductor crystals by X-ray diffraction," *J. Cryst. Growth*, vol. 135, pp. 71–77, 1994.

[67] Y. H. Lo, "New approach to grow pseudomorphic structures over the critical thickness," *Appl. Phys. Lett.*, vol. 59, p. 2311, 1991.

[68] W. J. Schaffer, M. D. Lind, S. P. Kowalczyk, and R. W. Grant, "Nucleation and strain relaxation at the InAs/GaAs(100) heterojunction," *J. Vac. Sci. Technol. B*, vol. 1, p. 688, 1983.

[69] A. M. Andrews, J. S. Speck, A. E. Romanov, M. Bobeth, and W. Pompe, "Modeling cross-hatch surface morphology in growing mismatched layers," *J. Appl. Phys.*, vol. 91, p. 1933, 2002.

[70] W.-S. Liu, Y.-T. Wang, W.-Y. Qiu, and C. Fang, "Carrier Dynamics of a Type-II Vertically Aligned InAs Quantum Dot Structure with a GaAsSb Strain-Reducing Layer," *Appl. Phys. Express*, vol. 6, p. 085001, 2013.

[71] O. L. Lazarenkova and A. A. Balandin, "Miniband formation in a quantum dot crystal," *J. Appl. Phys.*, vol. 89, p. 5509, 2001.

[72] T. B. Norris, K. Kim, J. Urayama, Z. K. Wu, J. Singh, and P. K. Bhattacharya, "Density and temperature dependence of carrier dynamics in self-organized InGaAs quantum dots," *J. Phys. D: Appl. Phys.*, vol. 38, pp. 2077–2087, 2005.

[73] T. Schmidt, K. Lischka, and W. Zulehner, "Excitation-power dependence of the near-band-edge photoluminescence of semiconductors," *Phys. Rev. B*, vol. 45, p. 8989, 1992.

[74] S. Sanguinetti, D. Colombo, M. Guzzi, E. Grilli, M. Gurioli, L. Seravalli, P. Frigeri, and S. Franchi, "Carrier thermodynamics in InAs⁄$In_xGa_{1-x}As$ quantum dots," *Phys. Rev. B*, vol. 74, p. 205302, 2006.

[75] Y. Qiu, P. Gogna, S. Forouhar, A. Stintz, and L. F. Lester, "High-performance InAs quantum-dot lasers near 1.3 μm," *Appl. Phys. Lett.*, vol. 79, p. 3570, 2001.

[76] K. Stewart, M. Buda, J. Wong-Leung, L. Fu, C. Jagadish, A. Stiff-Roberts, and P. Bhattacharya, "Influence of rapid thermal annealing on a 30 stack InAs/GaAs quantum dot infrared photodetector," *J. Appl. Phys.*, vol. 94, p. 5283, 2003.

[77] F. K. Tutu, I. R. Sellers, M. G. Peinado, C. E. Pastore, S. M. Willis, A. R. Watt, T. Wang, and H. Y. Liu, "Improved performance of multilayer InAs/GaAs quantum-dot solar cells using a high-growth-temperature GaAs spacer layer," *J. Appl. Phys.*, vol. 111, p. 046101, 2012.

[78] W.-T. Hsu, Y.-A. Liao, F.-C. Hsu, P.-C. Chiu, J.-I. Chyi, and W.-H. Chang, "Effects of GaAsSb capping layer thickness on the optical properties of InAs quantum dots," *Appl. Phys. Lett.*, vol. 99, p. 073108, 2011.

[79] J. Tatebayashi, N. Nuntawong, P. S. Wong, Y.-C. Xin, L. F. Lester, and D. L. Huffaker, "Strain compensation technique in self-assembled InAs/GaAs quantum dots for applications to photonic devices," *J. Phys. D: Appl. Phys.*, vol. 42, p. 073002, 2009.

[80] D. Y. Noh, Y. Hwu, J. H. Je, M. Hong, and J. P. Mannáerts, "Strain relaxation in Fe3(Al,Si)/GaAs: An xray scattering study," *Appl. Phys. Lett.*, vol. 68, p. 1528, 1996.

[81] H. Saito, K. Nishi, and S. Sugou, "Influence of GaAs capping on the optical properties of InGaAs/GaAs surface quantum dots with 1.5 μm emission," *Appl. Phys. Lett.*, vol. 73, p. 2742, 1998.

[82] S. Hatch, J. Wu, K. Sablon, P. Lam, M. Tang, Q. Jiang, and H. Liu, "InAs/GaAsSb quantum dot solar cells," *Opt. Express*, vol. 22, p. A679, 2014.

[83] J. F. Chen, R. S. Hsiao, M. F. Hsieh, J. S. Wang, and J. Y. Chi, "Effect of incorporating an InAlAs layer on electron emission in self-assembled InAs quantum dots," *J. Appl. Phys.*, vol. 99, p. 014303, 2006.

[84] J. S. Kim, P. W. Yu, J.-Y. Leem, M. Jeon, S. K. Noh, J. I. Lee, G. H. Kim, S.-K. Kang, J. S. Kim, and S. G. Kim, "Effects of high potential barrier on InAs quantum dots and wetting layer," *J. Appl. Phys.*, vol. 91, p. 5055, 2002.

[85] R. Jia, D. S. Jiang, H. Y. Liu, Y. Q. Wei, B. Xu, and Z. G. Wang, "Influence of combined InAlAs and InGaAs strain-reducing laser on luminescence properties of InAs/GaAs quantum dots," *J. Cryst. Growth*, vol. 234, pp. 354–358, 2002.

[86] K. A. Sablon, J. W. Little, K. A. Olver, Z. M. Wang, V. G. Dorogan, Y. I. Mazur, G. J. Salamo, and F. J. Towner, "Effects of AlGaAs energy barriers on InAs/GaAs quantum dot solar cells," *J. Appl. Phys.*, vol. 108, p. 074305, 2010.

[87] F. Guffarth, R. Heitz, a. Schliwa, O. Stier, N. Ledentsov, a. Kovsh, V. Ustinov, and D. Bimberg, "Strain engineering of self-organized InAs quantum dots," *Phys. Rev. B*, vol. 64, p. 085305, 2001.

[88] K. Feldrapp, R. Horbelt, R. Auer, and R. Brendel, "Thin-film (25.5 μm) solar cells from layer transfer using porous silicon with 32.7 mA/cm^2 short-circuit current density," *Prog. Photovolt: Res. Appl.*, vol. 11, pp. 105–112, 2003.

[89] N. M. Haegel, S. E. Williams, C. L. Frenzen, and C. Scandrett, "Minority carrier lifetime variations associated with misfit dislocation networks in heteroepitaxial GaInP," *Semicond. Sci. Technol.*, vol. 25, p. 055017, 2010.

[90] V. K. Yang, S. M. Ting, M. E. Groenert, M. T. Bulsara, M. T. Currie, C. W. Leitz, and E. A. Fitzgerald, "Comparison of luminescent efficiency of InGaAs quantum well structures grown on Si, GaAs, Ge, and SiGe virtual substrate," *J. Appl. Phys.*, vol. 93, p. 5095, 2003.

[91] J. W. Matthews and A. E. Blakeslee, "DEFECTS IN EPITAXIAL MULTILAYERS," *J. Cryst. Growth*, vol. 27, pp. 118–125, 1974.

[92] Y. Zhu, N. Jain, S. Vijayaraghavan, D. K. Mohata, S. Datta, D. Lubyshev, J. M. Fastenau, W. K. Liu, N. Monsegue, and M. K. Hudait, "Role of InAs and GaAs terminated heterointerfaces at source/channel on the mixed As-Sb staggered gap tunnel field effect transistor structures grown by molecular beam epitaxy," *J. Appl. Phys.*, vol. 112, p. 024306, 2012.

[93] S. M. Hu, "Misfit dislocations and critical thickness of heteroepitaxy," *J. Appl. Phys.*, vol. 69, p. 7901, 1991.

[94] S.-L. Weng, "Experimental studies of misfit dependence of critical layer thickness in pseudomorphic InGaAs single-strained quantum-well structures," *J. Appl. Phys.*, vol. 66, p. 2217, 1989.

[95] S. A. Ringel, J. A. Carlin, C. L. Andre, M. K. Hudait, M. Gonzalez, D. M. Wilt, E. B. Clark, P. Jenkins, D. Scheiman, A. Allerman, E. A. Fitzgerald, and C. W. Leitz, "Single-junction InGaP/GaAs solar cells grown on Si substrates with SiGe buffer layers," *Prog. Photovolt: Res. Appl.*, vol. 10, pp. 417–426, 2002.